International Journal of Greenhouse Gas Control 108 (2021) 103310

Contents lists available at ScienceDirect

International Journal of Greenhouse Gas Control

journal homepage: www.elsevier.com/locate/ijggc

Detection and quantification of CO_2 seepage in seawater using the stoichiometric C_{seep} method: Results from a recent subsea CO_2 release experiment in the North Sea

Abdirahman M. Omar [a,*], Maribel I. García-Ibáñez [a,1], Allison Schaap [d], Anna Oleynik [b], Mario Esposito [c], Emil Jeansson [a], Socratis Loucaides [d], Helmuth Thomas [e], Guttorm Alendal [b]

[a] NORCE, Norwegian Research Centre, Bjerknes Centre for Climate Research, Bergen, Norway
[b] Department of Mathematics, University of Bergen, Norway
[c] GEOMAR Helmholtz Centre for Ocean Research Kiel, Kiel, Germany
[d] National Oceanography Centre, Southampton, UK
[e] Institute of Carbon Cycles, Helmholtz Center Geesthacht, Geesthacht, Germany

ARTICLE INFO

Keywords:
Subsea CO_2 release
Seafloor CO_2 seepage monitoring
CO_2 seepage detection
Baseline C establishment

ABSTRACT

Carbon Capture and Storage (CCS) is a potential significant mitigation strategy to combat climate change and ocean acidification. The technology is well understood but its current implementation must be scaled up nearly by a hundredfold to become an effective tool that helps meet mitigation targets. Regulations require monitoring and verification at storage sites, and reliable monitoring strategies for detection and quantification of seepage of the stored carbon need to be developed. The C_{seep} method was developed for reliable determination of CO_2 seepage signal in seawater by estimating and filtering out natural variations in dissolved inorganic carbon (C). In this work, we analysed data from the first-ever subsea CO_2 release experiment performed in the north-western North Sea by the EU STEMM−CCS project. We successfully demonstrated the ability of the C_{seep} method to (i) predict natural C variations around the Goldeneye site over seasonal to interannual time scales; (ii) establish a process-based baseline C concentration with minimal variability; (iii) determine CO_2 seepage detection threshold (DT) to reliably differentiate released−CO_2 signal from natural variability and quantify released−CO_2 dissolved in the sampled seawater. DT values were around 20 % of the natural C variations indicating high sensitivity of the method. Moreover, with the availability of DT value, the identification of released−CO_2 required no pre-knowledge of seepage occurrence, but we used additional available information to assess the confidence of the results. Overall, the C_{seep} method features high sensitivity, automation suitability, and represents a powerful future monitoring tool both for large and confined marine areas.

1. Introduction

Carbon Capture and Storage (CCS) is a potential significant mitigation strategy to combat climate change and ocean acidification in climate change scenarios (e.g., van Vuuren et al., 2011; IPCC, 2013; Fuss et al., 2014). Three out of four 1.5 °C-consistent emission pathways published by the IPCC include CCS as well as bioenergy CCS (BECCS) as mitigation options (IPCC, 2018). However, the scale of current CCS implementation is insufficient to impcat the global climate, and thousands of large-scale CCS facilities need to be deployed by 2040 to meet mitigation targets (Global CCS institute, 2019). Moreover, the technology is in early stage of research, development, and demonstration (e.g., Hammond, 2018) and involves uncertainties and risks (e.g., Damen et al., 2006) that might raise ethical and governance issues, as is the case for other so-called climate geoengineering techniques (Lawrence et al., 2018).

Many potential CCS storage reservoirs are located below the seafloor (Blackford et al., 2017), and a number of subsea storage demonstration projects are in operation (IEAGHG, 2008; Jenkins, 2020). However, before subsea CO_2 storage can be carried out at industrial scales, potential ecological consequences and adverse environmental impacts of any unintended CO_2 seepages need to be identified. Therefore,

* Corresponding author.
E-mail address: abdir.omar@norceresearch.no (A.M. Omar).
[1] Now at Centre for Ocean and Atmospheric Sciences, School of Environmental Sciences, University of East Anglia, Norwich, UK.

https://doi.org/10.1016/j.ijggc.2021.103310
Received 17 August 2020; Received in revised form 8 March 2021; Accepted 15 March 2021
Available online 31 March 2021

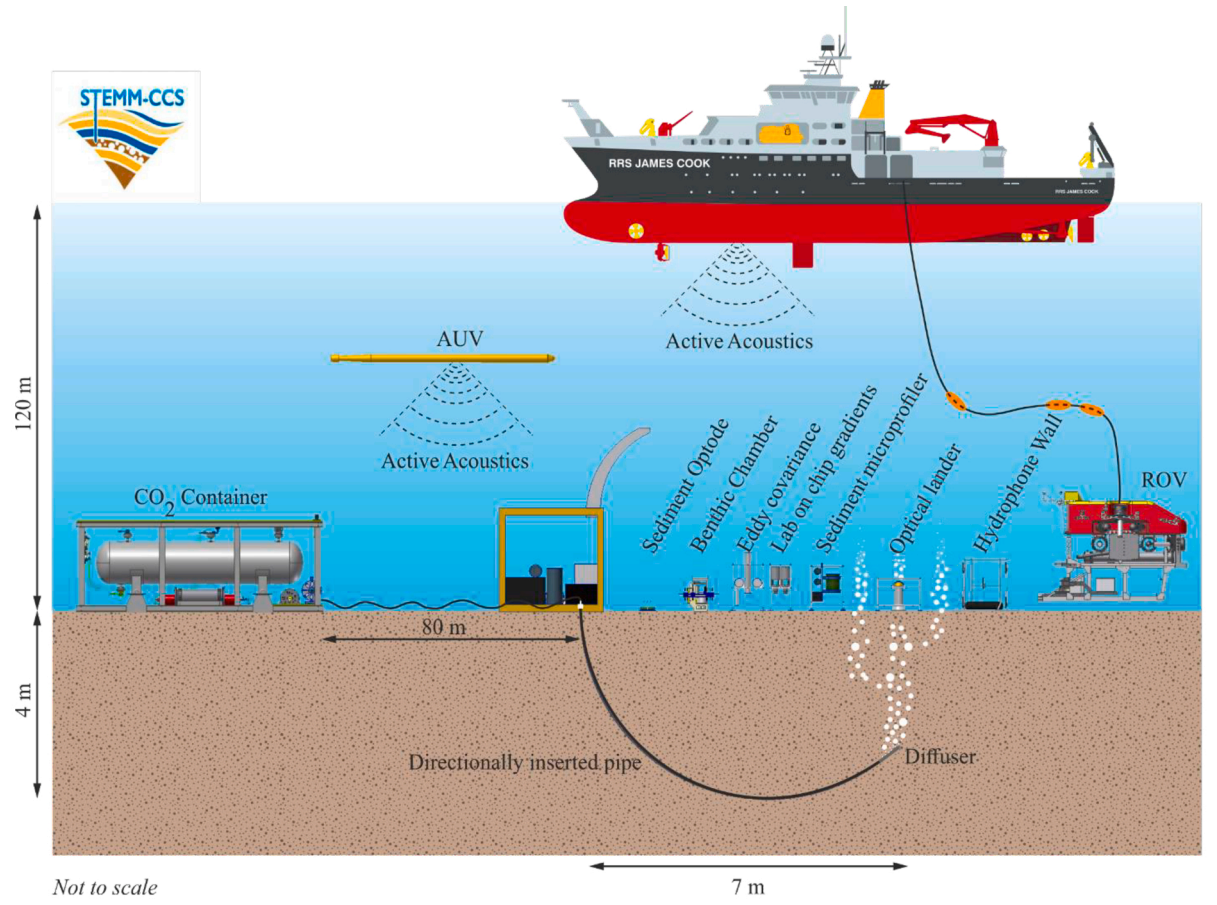

Fig. 1. Schematic illustrating the STEMM−CCS controlled CO_2 release experiment including some of the measurement technologies and platforms used. Image Courtesy C. Pearce, NOC.

monitoring and verification is required at storage sites by national and international regulations (e.g., U.S. EPA, 2010; European Commission, 2011; Dixon and Romanak, 2015), and reliable monitoring strategies for detection and quantification of seepage need to be developed.

Primary monitoring of storage reservoirs is based on seismic techniques imaging CO_2 through the overburden (Jenkins, 2020). However, the detection threshold of such techniques may be of the order of 10^3 t CO_2 (Jenkins, 2020), and they are prone to interpretation uncertainty (Schaaf and Bond, 2019). Therefore, possible seepage at low levels may not be detected by seismic techniques, and monitoring for seepage at the seafloor provides an important secondary strategy. The modelling work of Blackford et al. (2020) reported that release events can be detected at the seafloor at thresholds well below levels that would compromise storage performance or significantly damage the environment.

When CO_2 seeping through the seafloor dissolves into seawater, it goes through a series of reactions that ultimately increase the concentration of dissolved inorganic carbon (DIC; hereafter denoted as C for simplicity). Thus, the excess C dissolved in the seawater (C_{seep}) should, in principle, be readily quantified from the resulting change in C (ΔC). In practice, however, this is complicated by the fact that the dissolution of seepage CO_2 may be occurring on top of simultaneous C changes that result from natural processes, such as the formation/remineralization of organic matter and/or calcium carbonate ($CaCO_3$), mixing between water masses, and uptake of atmospheric CO_2. Thus, any natural parts of ΔC must be accounted for before the CO_2 seepage signal can be identified and C_{seep} accurately determined.

The challenge of distinguishing subsea CO_2 seepage signal from natural variability can be overcome using different techniques. Uchimoto et al. (2017; 2018) proposed a seepage CO_2 detection method based on site-specific covariance between partial pressure of CO_2 in seawater (pCO_2) and dissolved oxygen (DO). Blackford et al. (2017) proposed site-specific anomaly detection criteria that recognises unnatural rates of change in seawater CO_2 concentrations. Gundersen et al. (2020) demonstrated the use of machine learning techniques for detecting signals from a seep using data from seep simulations. The above techniques are concentration-based, meaning that they rely on measured concentrations to identify seepage signals without analysing the processes that govern the natural variations. Romanak et al. (2012) discussed the limitations of concentration-based monitoring and recommended process-based techniques, which identify drivers of the natural variability and estimate their magnitude. Specifically, process-based methods are able to address the sensitivity of seepage signal detection criteria to changes in the natural processes due to, for instance, climatic and/or ecosystem variations.

The EU project STEMM−CCS (https://www.stemm-ccs.eu) carried out a first of its kind CO_2 release experiment designed to imitate CO_2 seepage from an offshore storage site (Fig. 1). The details of different aspects of this unique experiment have been described elsewhere (e.g., Connelly et al., 2019; Dean et al., 2020; Esposito et al., 2021; Flohr et al., 2021). The experiment was carried out at the Goldeneye site (58 °N, 0.4 °W) in the North Sea where a controlled mixture of CO_2 and tracer gases was released into the sediments at 3 m below the seafloor. The suitability of existing and new methods for the monitoring, detection and assessment of potential environmental impacts of the CO_2 release were demonstrate/evaluated. Before the release experiment, the STEMM−CCS project conducted a number of cruises around the Goldeneye site in order to establish environmental and ecological baselines. The project also developed/further-developed novel chemical sensors

which have been utilized for data acquisition during both the baseline gathering and during the release experiment.

In this study, we use data from the STEMM−CCS release experiment to demonstrate the ability of the recently developed, process-based, C_{seep} method (Botnen et al., 2015; Omar et al., 2018) to (i) distinguish CO_2 seepage signal from the natural variability, and (ii) quantify the excess seepage CO_2 dissolved in the seawater, i.e., C_{seep}. The C_{seep} method (section 2) estimates the magnitude of the natural variations (ΔC_{nat}) and filters them out to facilitate the detection of CO_2 seepage signal. We demonstrate the aptness of the method to establish a baseline C concentration (C_b) and a detection threshold (DT) (section 3). We discuss the benefits of detecting seepage signals through the C_{seep} method (section 4), which is a promising marine monitoring tool: its implementation is flexible, it is suitable for automation, it can provide large area coverage, and it requires no pre-knowledge of CO_2 seepage occurrence (sections 5 and 6).

1.1. Variables of the seawater CO_2 system

The dissolution of CO_2 in seawater and subsequent equilibrium reactions form a complex chemical system (section 2), often referred to as the seawater CO_2 system, equilibrium properties of which are well characterised (e.g., Zeebe and Wolf-Gladrow, 2001). The seawater CO_2 system can be characterised by the following four measurable master variables (Dickson, 2010):

Total alkalinity (TA), which is related to the charge balance in seawater:

$$\begin{aligned} TA = {} & [HCO_3^-] + 2[CO_3^{2-}] \\ & + [B(OH)_4^-] + [OH^-] + [HPO_4^{2-}] + 2[PO_4^{3-}] + [SiO(OH)_3^-] + [HS^-] \\ & + 2[S^{2-}] + [NH_3] - [H^+]_F - [HSO_4^-] - [HF] - [H_3PO_4] \end{aligned} \quad (1)$$

where brackets denote concentrations. The bicarbonate and carbonate ions ($[HCO_3^-]$ and $[CO_3^{2-}]$) contribute about 96 % of the seawater TA.

Dissolved inorganic carbon (C), which is the sum of the concentrations of all forms of inorganic carbon dissolved in seawater:

$$C = [CO_2] + [HCO_3^-] + [CO_3^{2-}] \quad (2)$$

where $[CO_2]$ represent the sum of the concentrations of CO_2 in aqueous solution.

Partial pressure of CO_2 (pCO_2) in an air sample in equilibrium with the seawater sample:

$$pCO_2 = xCO_2 * p \quad (3)$$

where xCO_2 is the mole fraction of CO_2 in the gas phase and p is the total pressure.

pH_T (henceforth pH for simplicity) which represents the total hydrogen ion concentration in seawater:

$$pH = -\log[H^+]_T \quad (4).$$

The above master variables can be measured using a wide variety of techniques (Dickson, 2010) following standard operating procedures (Dickson et al., 2007). TA and C are traditionally determined by acidimetric titration and, currently, discrete sampling and benchtop instrumentation give the highest accuracy.

By measuring any two of the above-mentioned four master variables (along with temperature, salinity, pressure and the knowledge of other non−CO_2 acid-base systems in seawater), it is possible to calculate the remaining variables e.g., by using the CO2SYS software (van Heuven et al., 2011). Additionally, by selecting the appropriate two parameters for measurements, the uncertainties in the computed parameters can be held at the same order of magnitude as their experimental errors (Millero, 2007). Sensors that can autonomously measure pCO_2 and pH in situ at high frequency are commercially available and show satisfactory precision and accuracy (e.g., Bushinsky et al., 2019). Paired measurements of pH and pCO_2, however, are the least favoured since the computed TA and C values carry the highest uncertainty. Therefore, a major focus of the STEMM−CCS project was to develop new Lab-on-chip (LOC)-based sensor technologies to enable direct high-resolution in situ measurements of pH, TA and C. LOC-based sensors enable the automation of high performance wet-chemical analytical techniques offering high quality measurements usually only possible using benchtop laboratory instrumentation (Beaton et al., 2012; Clinton-Bailey et al., 2017; Rérolle et al., 2013).

Although measuring two of the four master variables gives the basis for a complete determination of the seawater CO_2 system, a process-based interpretation of the variability included in the data requires ancillary variables that are indicators for the governing processes. Examples of such variables include nutrients as indicators of biological activity, and salinity as an indicator of mixing between different water masses. Autonomous LOC sensors for the determination of nutrients (Beaton et al., 2012; Clinton-Bailey et al., 2017), and commercial off-the-shelf sensors (Sea-Bird Scientific) for temperature and salinity measurements were deployed on a number of platforms during the CO_2 release experiment to collect high-resolution in situ observations. Thus, the STEMM−CCS project demonstrated that high resolution data needed for the application of the C_{seep} methodology can be acquired by using cost-effective in situ sensors (section 4.1, Table 3).

2. Conceptual description of the C_{seep} method

When seepage CO_2 dissolves in seawater, it reacts with the water forming carbonic acid (H_2CO_3), which rapidly dissociates into bicarbonate ions (Eq. 5), which in turn can also dissociate into carbonate ions (Eq. 6) according to the following equilibrium reactions:

$$CO_2 + H_2O \leftrightarrow H_2CO_3 \leftrightarrow HCO_3^- + H^+ \quad (5)$$

$$HCO_3^- \leftrightarrow CO_3^{2-} + H^+ \quad (6).$$

In terms of measurable variables, the net result of the above reactions is an increase in C and a decrease in pH. Thus, any seepage CO_2 dissolved in seawater should, in principle, be readily quantified from the resulting concentration changes. However, C in seawater is also influenced by natural processes, such as photosynthesis/respiration, biosynthesis/dissolution of $CaCO_3$ and changes in temperature and salinity. Therefore, the approach of the C_{seep} method is to quantify the natural variability and filter it out to facilitate the detection of CO_2 seepage dissolved in seawater. To achieve this, the method conveniently focuses on changes in C because this variable tracks concentration changes in all of the inorganic carbon species dissolved in seawater (Eq. 2) regardless of whether the changes are due to natural processes or to CO_2 seepage. Additionally, C mixes conservatively in the absence of biological activity.

The amount of C in seawater is set largely set by equilibrium reactions whilst natural processes produce deviations through various sinks and sources of seawater constituents. Therefore, the C_{seep} method assumes that there is an essentially invariant theoretical baseline seawater C (C_b), which is dictated by the equilibrium history and physical properties of the water parcel, and over which fluctuations created by natural processes (ΔC_{nat}) and/or CO_2 seepage (C_{seep}) are superimposed so that:

$$C = C_b + \Delta C_{nat} + C_{seep} \quad (7)$$

where C is the measured background concentration and C_b is assumed to be invariant. The terms on the right hand-side of Eq. 7 are determined in two steps (see also Fig. 4):

1 Acquisition of background measurements of C (and ancillary parameters) that are influenced by ΔC_{nat} only and not by CO_2 seepage,

Table 1
Overview of the data used to establish the baseline C (C_b) around the Goldeneye site (Fig. 3).

Dataset name	Measured parameters	Accuracy	Sampling mode	Sampling period	Sample depth	Data originator(s) (contact person)
Historical Baseline Cruise Data	C (μmol kg^{-1}) TA (μmol kg^{-1}) T (°C) S PO_4 (μmol kg^{-1}) NO_3 (μmol kg^{-1})	0.08 % 0.1 % 0.00016 °C 0.3 % 5 % 3 %	Bottle data	Nov 2001, Feb 2002, May 2002, Aug 2005, 2008, and 2011	Deepest sample, 10–20 m above the sea floor	GLODAPv2 [§](H. Thomas)
POS518 and POS527	C (μmol kg^{-1}) TA (μmol kg^{-1}) T (°C) S PO_4 (μmol kg^{-1}) NO_3 (μmol kg^{-1})	0.08 % 1 % 0.00016 °C 0.3 % 5 % 3 %	Bottle data	Aug 2018 and Oct 2017	Deepest sample, 10–20 m above the sea floor	STEMM-CCS (M. Esposito)
JC180BL	TA (μmol kg^{-1}) T (°C) PO_4 (μmol kg^{-1}) pH C[†] Current (direction and speed)	0.12 % 10 % 0.01 0.4 %**	Sensor data	Apr-May 2019	126 m	STEMM-CCS (A. Schaap)

C = dissolved inorganic carbon; TA = total alkalinity; S = salinity; T = temperature; PO_4=phosphate; and NO_3=nitrate.
[†] C computed from pH and mean sensor TA using the CO2SYS program (van Heuven et al., 2011) and dissociation constants of Millero et al (2006).
[**] Estimated according to Dickson and Rilley (1978).
[§] Olsen et al. (2016).

i.e., $C_{seep} = 0$. Based on these data, set up a site-specific model to estimate ΔC_{nat} and determine C_b according to:

$$C_b = C^B - \Delta C^B_{nat} \quad (8)$$

where the superscript 'B' stands for background whereas the subscript 'b' stands for baseline.

2 Application of the model of step (1) to C measurements from the site-monitoring to determine the sum of C_b and C_{seep} (if any seepage occurred) according to:

$$C_{seep} = C^M - \Delta C^M_{nat} - C_b \quad (9)$$

where the superscript 'M' stands for site−monitoring.

Note the important distinction between C^B and C_b. The former is fluctuating due changes in ΔC^B_{nat} and, thus, depends on time and location whereas the latter is theoretically invariant. In practice, however, the errors in calculating ΔC^B_{nat} affect the values of C_b values so that they include some variability. This will be referred to as the "remnant variability". Similarly, errors in calculating ΔC^M_{nat} and C_b affect C_{seep}. In the following section we detail the determination of C_b, and analyse its remnant variability and its effects on C_{seep} determination.

3. Establishing C_b for the Goldeneye site

As mentioned in the previous section, the main purpose of establishing C_b is to facilitate reliable detection of seepage CO_2 signal and quantification of C_{seep} by comparing baseline and monitoring data. However, baseline determination has its own value. For instance, by analysing C_b values obtained from Eq. 8 we can check our understanding of the natural variability of C in the study area. A good understanding of the natural variability of C results in a successful characterization of ΔC^B_{nat}, which, in turn, results in confident C_b values. Moreover, by determining C_b over large spatial and temporal scales we can analyse the variability in C_b in relation to sampling location/time. This, in turn, allows us to examine over what spatial and temporal scales we can expect an invariant C_b. Furthermore, by computing the difference between C_b values obtained for different stations/times we yield an estimate on the uncertainty in C_{seep}, which is a measure of the detection threshold for seepage CO_2 signal. All these aspects are detailed in following subsections.

3.1. Baseline data

For the determination of C_b (Eq. 8) we used water column measurements from the area at and around the Goldeneye site (Fig. 3). An overview of the datasets is shown in Table 1, and it comprises publicly available historical data as well as new data gathered within the STEMM−CCS project. The historical dataset was obtained during multi-year (2001–2002, 2005, 2008, and 2011) basin-wide cruises using discrete sampling and shipboard analyses (Clargo et al., 2015; Thomas, 2002). We used a 2-by-2.5-degree subset of this historical cruise dataset to characterize the large-scale spatiotemporal variability around the Goldeneye site. The new dataset (2017–2019) comprises both cruise data and high-frequency in situ sensors data. The cruise data were gathered onboard *RV Poseidon* using samples drawn from Niskin bottles mounted on a CDT-rosette (Fig. 2A). These water samples were analysed onboard using benchtop instrumentations (Fig. 2B and D) as described in Esposito et al. (2021). We used the data acquired within the geographical area of 0.35° Lon x 0.1° Lat (Fig. 3) in October 2017 (POS518) and August 2018 (POS527).

The high resolution data were obtained from sensors attached to seabed baseline lander (Fig. 2C) deployed by *RV James Cook* at ~58 °N, 0.3 °W, between April and May 2019, measuring at a two-hourly sampling frequency. These data will be henceforth referred to as the JC180BL dataset.

Our analyses focus on the deep samples (up to 10−20 m above the seafloor) where the CO_2 seepage signals are expected to appear first.

3.2. Determination of C_b through modelling the natural variability

The processes assumed to govern the natural variability of the seawater CO_2 system around the Goldeneye site are summarized in Fig. 4. They include (i) biological processes (ΔC_{bio}) that comprise photosynthesis/respiration (organic matter cycling; ΔC_{omc}) and formation/dissolution of $CaCO_3$ ($CaCO_3$ cycling; ΔC_{CaCO3}), (ii) mixing of water masses (ΔC_{mix}), and (iii) air-sea gas exchange (ΔC_{ase}) including oceanic

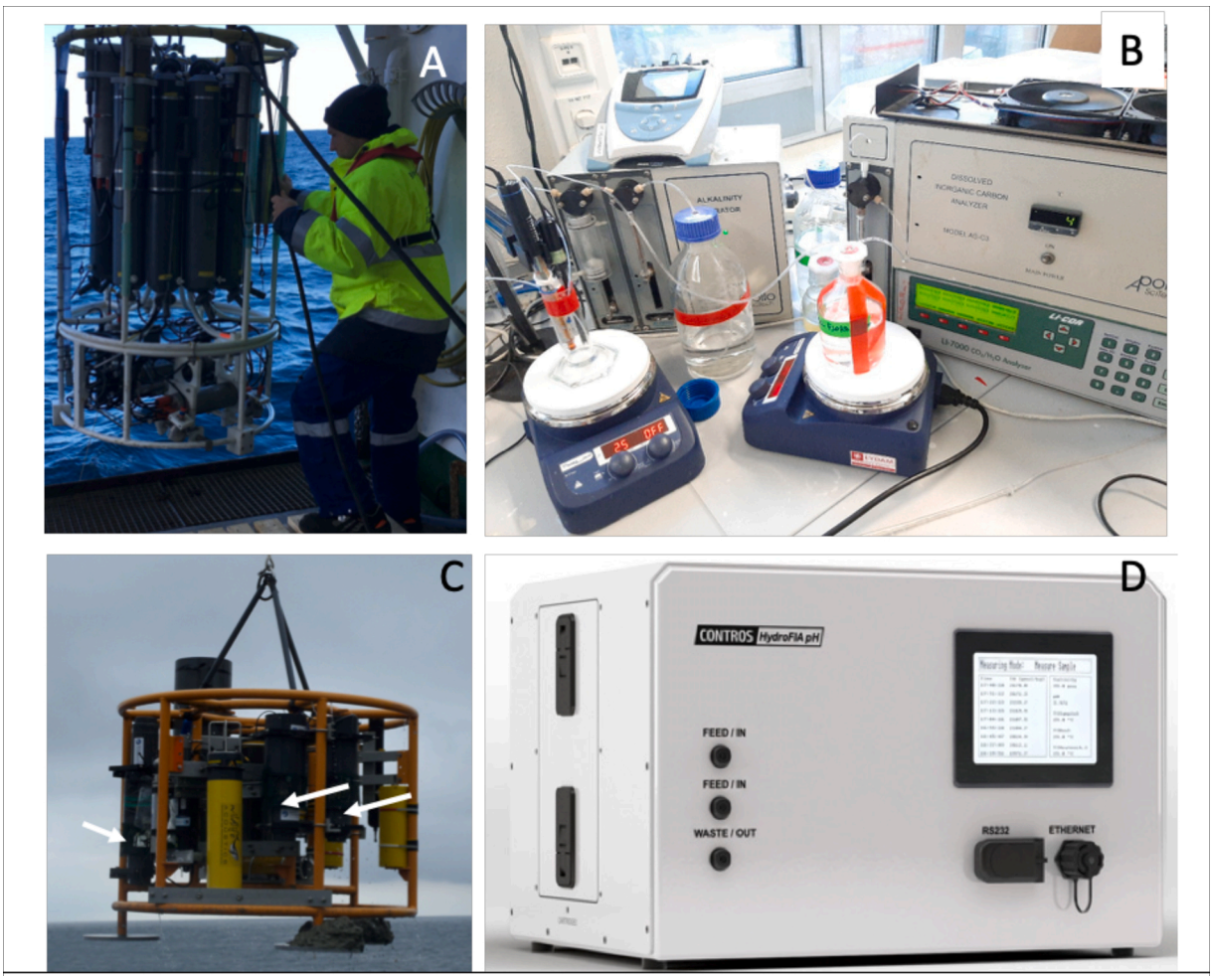

Fig. 2. A) Water sampler CTD-rosette with Niskin bottles used for discrete seawater sampling during the *RV Poseidon* cruises. (B and D) Benchtop instrumentation used for the determination of C and TA during the *RV Poseidon* cruises (Table 1). (C) The seabed Baseline Lander with integrated biogeochemical LOC sensors attached (white arrows) being deployed from *RV James Cook* in May 2019.

uptake of anthropogenic CO_2. In the context of this study, the oceanic uptake of anthropogenic CO_2 from the atmosphere is considered a natural process, i.e., a process that is not influenced by the subsea seepage. Therefore, the ΔC_{nat} term in Eq. 8 consists of contributions driven by biology (ΔC_{bio}), air-sea gas exchange (ΔC_{ase}), and mixing (ΔC_{mix}). Furthermore, as indicated in Fig. 4, the contributions of ΔC_{nat} are parameterized through a combination of changes in measured variables relative to some arbitrary reference values (Table 2), stoichiometric ratios, and empirical constants.

The details of how the contributions ΔC_{omc}, ΔC_{CaCO3}, ΔC_{mix}, and ΔC_{ase} are computed from the model parameters are given in Appendix A. Once the above contributions are determined, we obtain an estimate of ΔC_{nat} ($= \Delta C_{omc} + \Delta C_{CaCO_3} + \Delta C_{mix} + \Delta C_{ase}$), and then evaluate Eq. 8 to estimate C_b.

The mean values and standard deviations for ΔC_{omc}, ΔC_{CaCO3}, ΔC_{mix}, and ΔC_{ase} are shown in Table 2. In terms of mean values, the most influential contributions are, in decreasing order, ΔC_{omc}, ΔC_{mix}, ΔC_{ase}, and ΔC_{CaCO3}. In terms of contributions to ΔC_{nat} variability, the contribution order changes to ΔC_{omc}, ΔC_{mix}, ΔC_{CaCO3}, and ΔC_{ase} in decreasing order. For details of the above contributions see Fig. A1 in Appendix A.

The variability in C^B, ΔC^B_{nat}, and C_b is compared in Fig. 5. C^B varies on average between 2090 and 2180 µmol kg^{-1}, with mean and standard deviation values of 2160 ± 17 µmol kg^{-1} (Fig. 5A), confirming the highly dynamic CO_2 system parameters known for shelf regions (e.g., DeGrandpre et al., 1997). Changes observed at any given station arise from temporal changes occurring on the sub-seasonal to interannual time scales. The historical data captures the seasonal to interannual variability, whereas the sub-seasonal changes are captured by the JC180BL data, which were acquired over 22 days (29 Apr–21 May). Spatial changes, on the other hand, are observed between different stations and their magnitude is comparable to the temporal changes. Another noticeable feature is the lower C^B values observed in the coastal stations (Fig. 5A; stations 49, 50, 55, and 75, station locations shown Fig. 3), which are due to the combination of lower salinity and higher primary production (Fig. A1B). The average amplitude of the variability in ΔC^B_{nat} (85 µmol kg^{-1}, Fig. 5B) closely matches that in C^B (90 µmol kg^{-1}, Fig. 5A). Therefore, the average variability in C_b ($= C^B - \Delta C^B_{nat}$) is substantially reduced (35 µmol kg^{-1}, Fig. 5C) being 60 % less variable than C^B. Furthermore, C_b reduces not only the station-to-station variations in C^B (shorter boxes in Fig. 5C compared to those in Fig. 5A) but also the variability within each station (difference between individual boxes Fig. 5C compared to those in Fig. 5A). This is because the variations in individual boxes of C^B and ΔC^B_{nat} partially cancel out.

In summary, Fig. 5 demonstrates that the application of the C_{seep} method substantially reduces the dependency of C_b on time and location, although it does not completely eliminate the spatiotemporal variability. Furthermore, the spatial extent of the study area does not seem to explain the remnant variability in C_b. This can be seen in Fig. 5C, where the range in C_b values computed for station 56, JC180BL, POS518, and POS527 brackets the entire remnant variability despite these data being acquired in quite close locations (Fig. 3). Possible

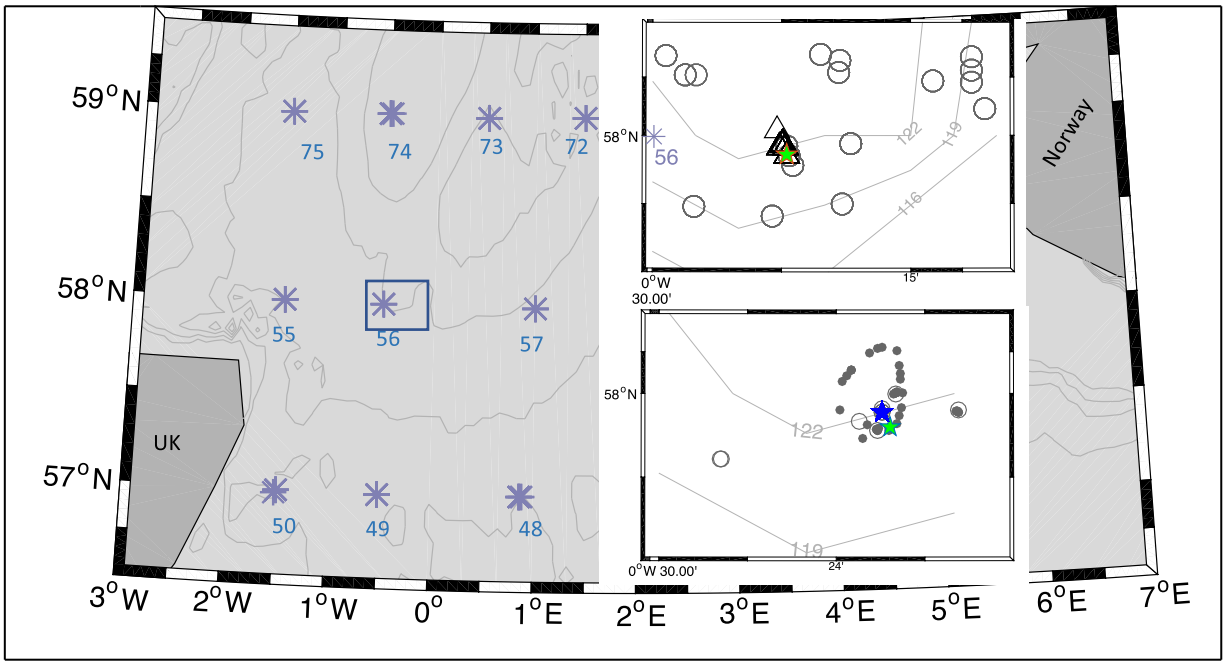

Fig. 3. Study area in the North Sea centred around the Goldeneye site (58 °N, 0.4 °W, rectangle). Also shown are depth contours (in m) and the locations sampled during historical cruises (asterisks) and baseline cruises (rectangle). **Upper inset:** detailed positions and depth contours of STEMM–CCS seabed baseline lander (JC180BL, green star), which is about 2 km east of station 56 of the historical cruises (asterisk), and sampling locations of the STEMM–CCS baseline cruises (POS518, triangles; POS527, circles). **Bottom inset:** detailed map of the area around the CO_2 release experiment site and the sampling locations during monitoring the released–CO_2 by the POS534 cruise (dots = sampling through pumping; circles = sampling from Niskin bottles) and by the JC180BBL lander (blue star). The latter was deployed ~2.6 m south of the centre of the CO_2 bubble streams. Also shown is the position of the JC180BL baseline lander (green star), which was deployed 375 m southeast of the CO_2 release point.

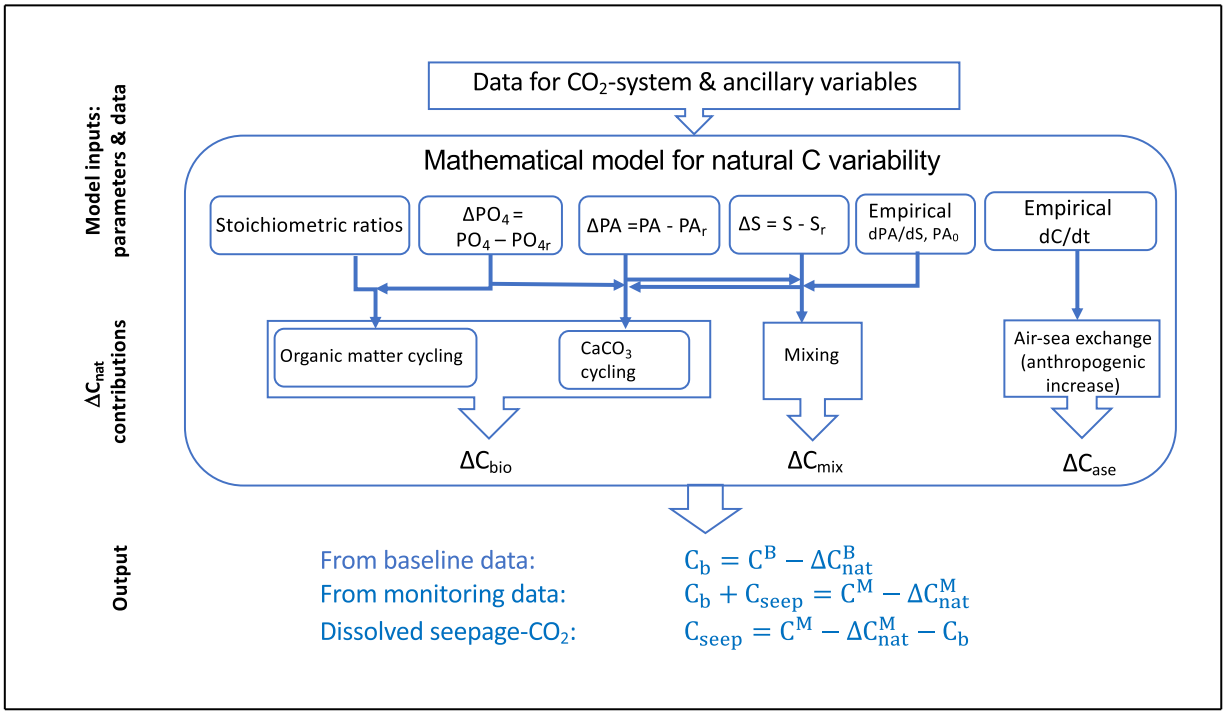

Fig. 4. Box diagram showing the required data and parameters for modelling the contributions of natural C variability (ΔC_{nat}). Also indicated are the outputs of the mathematical model for baseline and monitoring data, and that C_{seep} is determined as the difference of these outputs. In the model parameters, subscripts r denotes reference values, and Δ-values are computed as the difference: measured minus reference.
PA: is potential alkalinity i.e. TA from which the influence of organic matter is eliminated (Eq. A3, Appendix) dPA/dS: is change in PA resulting from salinity changes; PA_0: is the PA concentration at S = 0, i.e., in freshwater; dC/dt: is the annual C increase due to oceanic uptake of CO_2 from the atmosphere.

Table 2
The first part of the table shows arbitrary reference values to which all measured data in this work have been adjusted to. Mean values and standard deviations of the contributions of ΔC_{nat} are shown in the second part (see Appendix A for a boxplot of ΔC_{omc}, ΔC_{CaCO3}, ΔC_{mix}, and ΔC_{ase}).

Parameter	Reference value	Note
S	35.1	
PO_4 (μmol kg^{-1})	0.62	Mean values of the historical data
PA (μmol kg^{-1})	2323	
Year	2010	Close to median of the sampling years, 2011.

Dataset	Mean and STD values of ΔC_{nat} contributions (μmol kg^{-1})			
	ΔC_{omc}	ΔC_{CaCO3}	ΔC_{mix}	ΔC_{ase}
POS518	11 ± 8.0	2.4 ± 6.6	9.3 ± 1.0	8.4 ± 0.0
POS527	4.0 ± 6.0	2.3 ± 6.3	−3.9 ± 1.4	9.6 ± 0.0
Historical cruises	0.5 ± 21	0.0 ± 4.9	0.1 ± 13	−6.6 ± 4.1
JC180BL	−15 ± 0.0	8.9 ± 0.8	0.11 ± 1.6	10.8 ± 0.0

PA = potential total alkalinity, defined by Eq. A3 in Appendix A.

causes of remnant variability in C_b are explored in the next subsection.

3.3. Evaluation of the uncertainty in C_{seep} and detection threshold

The remnant variation in C_b (Fig. 3C) is due to imperfection of the model for ΔC^B_{nat} (Eqs. A1-A8) and errors in the model input, i.e., errors in the measured variables (Table 1) and in the estimates of dC/dt (1.2 ± 0.3 μmol kg^{-1} yr^{-1}), R_{CP} (117 ± 16), dPA/dS (67.5 ± 7.4 μmol kg^{-1}), and PA_0 (-46 ± 262 μmol kg^{-1}). We used the historical data to estimate the total error introduced into C_{seep} (E_{Cseep}) by the above uncertainties and due to the observed station-to-station differences in C_b (Fig. 5C). To achieve this, we first arbitrarily considered station 57 as a baseline station and the remaining stations as monitoring stations. Since there was no seepage in the area when the historical data were acquired (2001–2011) every station should, in principle, have the same C_b as station 57 so that $C_{seep} = 0$. However, the aforementioned uncertainties and remnant variability in C_b will introduce an error such that:

$$C_{seep} = C_b^{57} - C_b^x + E_{Cseep} \quad (10)$$

where *x* is any of the station numbers shown in Fig. 3 different from 57.

To estimate E_{Cseep} we used Monte Carlo (MC) simulations by

Table 3
Overview of the released−CO_2 monitoring data used to compute C_{seep} values at the Goldeneye site (Fig. 3).

Dataset name	Measured parameters	Accuracy	Sampling mode	Sampling period	Sample depth	Data originator(s) (contact person)
P POS534P and POS534B	C (μmol kg^{-1}) TA (μmol kg^{-1}) T (°C) S PO_4 (μmol kg^{-1}) NO_3 (μmol kg^{-1}) TA (μmol kg^{-1}) T (°C)	0.08 % 0.1 % 0.00016 °C 0.3 % 0.05 % 3% 0.12 %	Niskin bottles or continuous pumping	May 10–20, 2019	115–120 m	STEMM-CCS project (M. Esposito)
JC180BBL	S PO_4 (μmol kg^{-1}) pH C† Current (direction and speed)	0.3 % 10 % 0.01 0.4 %**	In situ, high frequency (every 20 min)	May 8–22, 2019	120 m	STEMM-CCS project (A. Schaap)

C = dissolved inorganic carbon; TA = total alkalinity; S = salinity; T = temperature; PO_4=phosphate; and NO_3=nitrate.
† C computed from pH and mean sensor TA using the CO2SYS program (van Heuven et al., 2011) and dissociation constants of Millero et al (2006).
** Estimated according to Dickson and Rilley (1978).

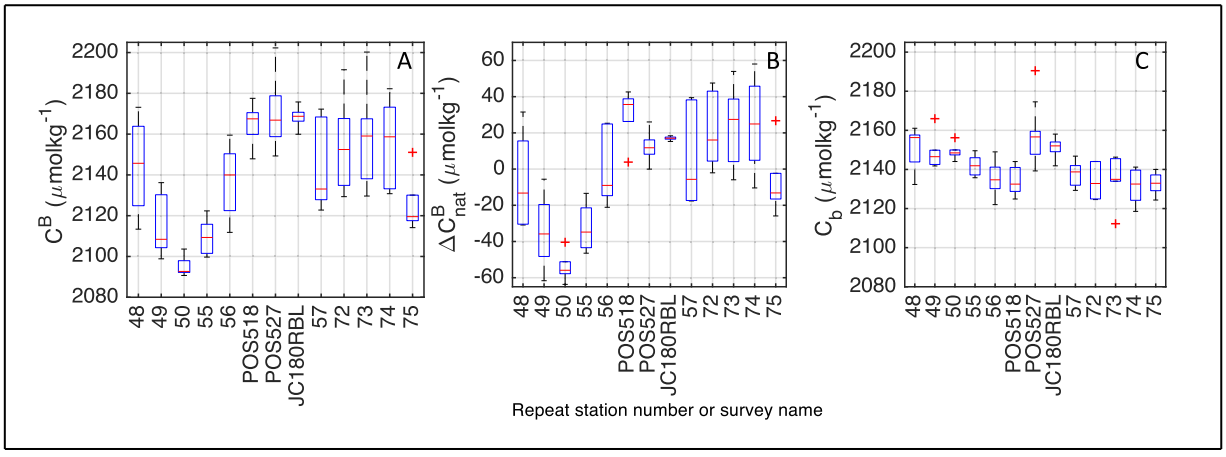

Fig. 5. Boxplots of (A) C^B, (B) ΔC^B_{nat}, and (C) C_b as a function of sampling station number or survey name. For each box, the central mark is the median, the edges of the box are the 25th and 75th percentiles, the whiskers extend to the most extreme data points not considered outliers, and outliers are individual crosses. Note that data from POS518, POS527, and JC180BL are shown next to station 56 because all these data were acquired from very close locations (Fig. 3). A comparison between panels (A) and (C) reveals how the implementation of the C_{seep} methodology minimises natural variations in C_b temporally (height of individual boxes) and spatially (difference between individual boxes).

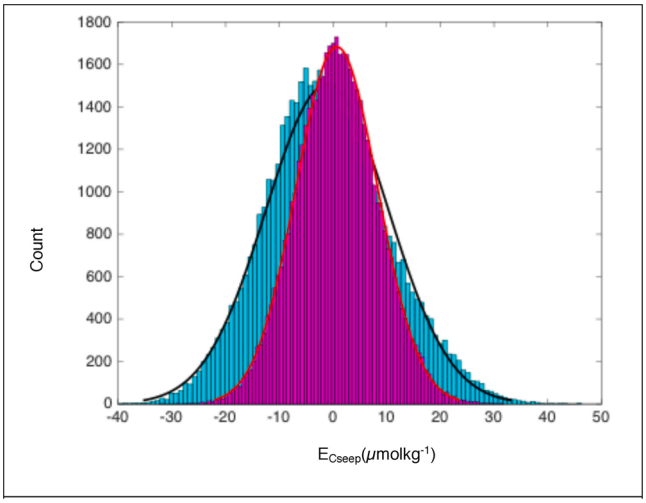

Fig. 6. Histograms of E_{Cseep} and normal distributions fitted to them for two situations: when C_b is held at its mean and changes are due to individual uncertainties only (red curve and magenta bars) versus when C_b changes due to both the remnant variability (Fig. 5C) and individual uncertainties in model inputs (black curve and cyan bars). In each case, the histograms are obtained with 50,000 evaluations of the underlying model (Eqs. A1–A8; Fig. 4).

evaluating the underlying model (Eqs. A1–A8; Fig. 4) 50,000 times, i.e., 1000 simulations for each of 50 unique model inputs. We chose MC simulations as an easier alternative for the traditional error propagation by differentiation and summations (Anderson, 1976) which would be rather tedious to program. During the simulations individual uncertainties (with magnitudes as given above and in Table 1) were randomly sampled from normal distributions and added to model inputs which were at their mean values.

The distribution of E_{Cseep} values driven by the individual uncertainties is well approximated by a normal distribution with a mean and standard deviation of 0.7 ± 7.6 μmol kg^{-1} (Fig. 6; red curve and magenta bars). For comparison, we estimated the E_{Cseep} values driven by the remnant variability in the historical C_b values (Fig. 5C, for station numbers 48–50, 55–57, and 72–75). To achieve this, we evaluated the underlying model by randomly sampling model inputs from normal distributions with means equal to the observed data and uncertainty set to zero. The resulting E_{Cseep} distribution is well approximated by a normal distribution with a mean and standard deviation of -1.0 ± 11.4 μmol kg^{-1} (Fig. 6; black curve and cyan bars).

From the above comparison we deduce that remnant variability in the historical C_b values (Fig. 5C), which results from all kinds of model imperfections, produces E_{Cseep} values with 1-STD of ±11.4 μmol kg^{-1} of which 67 % (7.6/11.4) are due to individual uncertainties in the model inputs.

We also used the Monte Carlo simulation described above to assess the influence of the individual uncertainties in the distribution of C_b. This time we simulated C_b instead of E_{Cseep}, by holding all model inputs at their mean values and adding to them randomly sampled individual uncertainties. The resulting C_b values were well approximated by a normal distribution with a mean and standard deviation of 2142 ± 4.7 μmol kg^{-1}. The remnant variability observed in the historical C_b values (Fig. 5C; for station numbers 48–50, 55–57, and 72–75) could be approximated by a normal distribution with mean and standard deviation of 2140 ± 10.7 μmol kg^{-1}. The individual uncertainties in the model inputs, therefore, account for 44 % (4.7/10.7) of the remnant variability in historical C_b value and the rest must be ascribed to processes/factors not resolved by our model for ΔC_{nat}. Two possible candidates of such factors include inter-laboratory differences in C measurements, which can be up to 10 μmol kg^{-1} (Bockmon and Dickson, 2015), and differences in sampling procedures. This may introduce systematic errors so that the uncertainty in C increases from 1 % (Table 2) to maximum 5 % i.e. ~ 10 μmol kg^{-1}. In fact, we were able to reproduce the whole remnant variability observed in C_b (1-STD = ±11 μmol kg^{-1}; Fig. 5C) by repeating the Monte Carlo simulations with a C^B uncertainty of 5 %. From this analysis, we conclude that the processes included in our underlying model (Fig. 4) are adequate to explain the natural C fluctuations in the study area, and the observed remnant variability in C_b arises

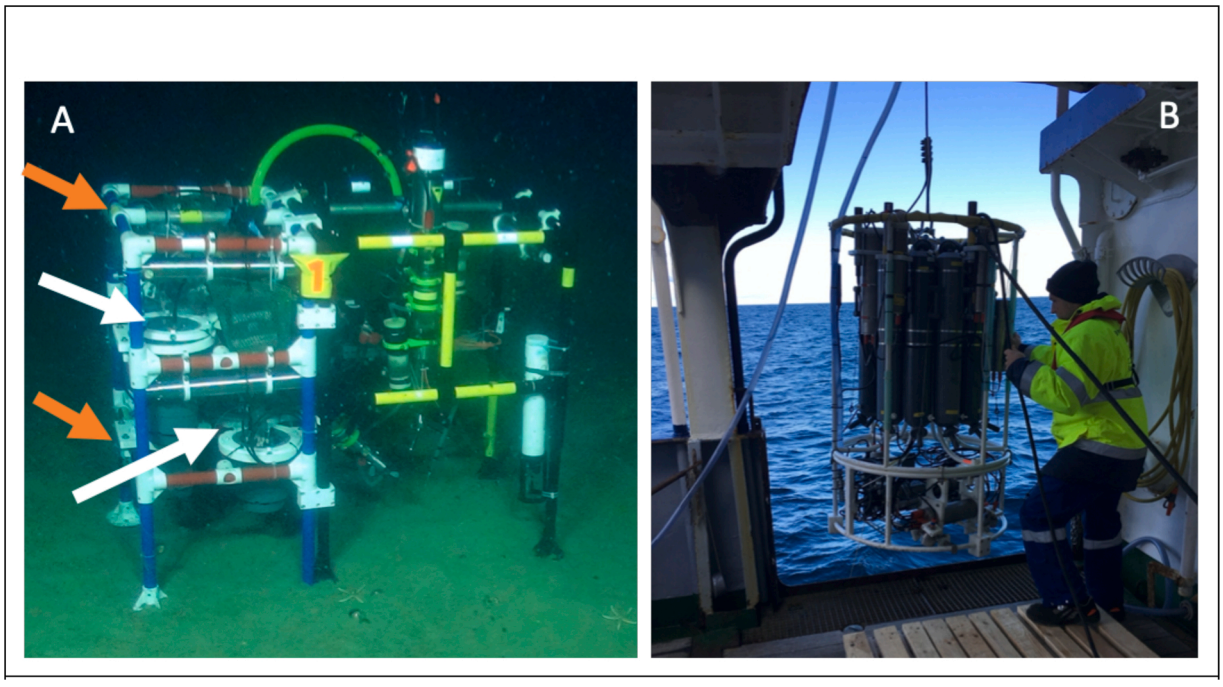

Fig. 7. (A) Benthic lander with the LOC sensors (white arrows) attached with inlets (red arrows) at 87 and 17 cm above the seafloor to monitor CO_2 plume in the benthic boundary layer. (B) A towed Video-CTD water sampler rosette being deployed for continuous water sampling using an attached underwater pump and 1-inch tubing/hose. A three-way tube connector was installed at the onboard part of the tubing in order to split the flow and allow for discrete seawater sample collection.

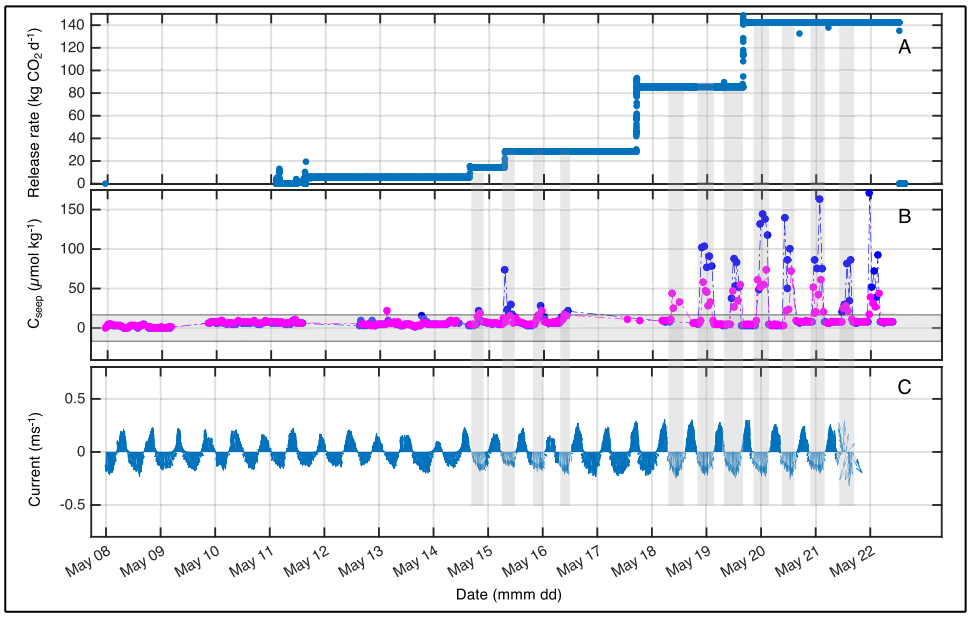

Fig. 8. Temporal development of: (A) flow rate of the released CO_2 measured at the tank; (B) C_{seep}, i.e., the excess C resulting from the released−CO_2 dissolved into the seawater sampled at 17 cm (blue) and 87 cm (magenta) above seafloor, respectively; and (C) water current velocity (positive values to the north). Vertical shaded bars indicate the alignment of CO_2 release rate, C_{seep} maxima, and current direction. The horizontal shaded bar indicates the threshold for confidently detecting the signal of CO_2 release in the seawater.

mainly from uncertainties in model inputs.

Based on the above results, we define the detection threshold (DT), over which C_{seep} values will be interpreted as CO_2 seepage signal, for two situations. If E_{Cseep} is affected by only individual uncertainties in model inputs then a DT = 15.2 µmol kg^{-1} (mean E_{Cseep} plus two standard deviations from the red curve in Fig. 6) will be used. On the other hand, when E_{Cseep} is expected to be influenced by both systematic errors and individual uncertainties in model inputs then DT = 24.8 µmol kg^{-1} (mean E_{Cseep} plus two standard deviations from the black curve in Fig. 6) will be used. The effect of changing DT to 1-STD or 3-STD is discussed in section 5.1.

4. Detection and quantification of dissolved released−CO_2

4.1. Monitoring data of the CO_2 release

For the computation of C_{seep} (Eq. 9), we used two C^M datasets collected during the monitoring of the CO_2 release (Table 1). The first is a high-frequency dataset acquired by LOC sensors mounted on a lander (Fig. 7A; Flohr et al., 2021) situated on the seafloor about 2.6 m to the south of the centre of the CO_2 bubble plumes. The data obtained by these sensors, which were deployed by *RV James Cook* to monitor the CO_2 bubble plume in the benthic boundary layer (BBL), will be henceforth referred to as the JC180BBL dataset. The sensors on this lander had two inlets for seawater, one at 17 cm above the seafloor and one at 87 cm above the seafloor. The sensor alternated between these two inlets and each measurement took 10 min. Here we used data sampled from both the inlets.

The second dataset is data gathered during a cruise with *RV Poseidon* using towed video-CTD (Fig. 7B) with an attached water pump to continuously monitor parameters in the water column around and above the CO_2 release site (Fig. 3, lower inset, dots). This technique has been described in detail in Linke et al. (2015) and Schmidt et al. (2015). Briefly, the 1-inch inlet tubing connected to an underwater pump was attached to the lower part of the video-CTD frame and the water was continuously pumped at a flow rate of about 30 l min^{-1} to sample from specific water depths. A three-way tube connector was installed to split the flow and allow for discrete water sample collection and later on-board analysis.

These observations were made during a full tidal cycle on May 13–14, 16–17, and 19–20, 2019 (Schmidt, 2019). Water column measurements sampled with Niskin bottles were also conducted during the *RV Poseidon* cruise (POS534; Fig. 3, lower inset, circles), both above the CO_2 release site (May 13–14, 16–17, and 19–20) and few kilometres away from the site (May 10–13). The cruise dataset will be referred to as POS534P or POS534B, where P and B denote sampling through pumping or through Niskin bottles, respectively. For this dataset, our analyses focus on the samples taken from 109 m or deeper, i.e., maximum ≈10 m above the seafloor where the strongest signal of the released−CO_2 is expected.

For both datasets, we include data acquired before the start of the CO_2 release to be able to assess if the application of the C_{seep} method results false positives, i.e., identify false released−CO_2 signals.

4.2. C_{seep} computed from high-frequency sensor data

C_{seep} was determined according to Eq. 9, using the high-frequency CO_2 release monitoring dataset (JC180BBL), ΔC^M_{nat} computed for the same dataset, and an average C_b value determined from the high-frequency baseline dataset (JC180BL). During the computations of ΔC^M_{nat} and C_b some data quality and paucities were circumvented as detailed in Appendix B. Since JC180BBL and JC180BL datasets were acquired simultaneously (but at different locations; Fig. 3) using the same sensor technology, we applied DT_{sensor} = 16.6 µmol kg^{-1} as discussed in section 3.3. In other words, only C_{seep} values larger than DT_{sensor} were confidently interpreted as a signal of released−CO_2.

The temporal development of C_{seep} together with those of the released−CO_2 rate and water movement (velocity) are shown in Fig. 8. Notably, prior to the onset of the CO_2 release, e.g., May 8–9, the C_{seep} values are close to zero (2.4 ± 2.3 µmol kg^{-1}) as expected since no released−CO_2 was dissolved in the seawater. C_{seep} values that are consistently above DT_{sensor} start to appear on May 15, when the released−CO_2 rate was ≥ 15 kg d^{-1}. After that date, the CO_2 release rate was even higher and elevated/extreme C_{seep} values ranging from 40 to 160 µmol kg^{-1} regularly appeared and their peak values generally scaled with rate of the CO_2 release. Moreover, the elevated C_{seep} values occurred whenever the current direction was southwards, i.e., aligned with the direction of the sensor location relative to the CO_2 bubble stream through the seafloor (Fig. 3, caption). On the basis of the above observations, we conclude that the C_{seep} method is able to detect the released−CO_2 signal in addition to quantifying the concentration of excess carbon dissolved in the sampled seawater. Moreover, the method

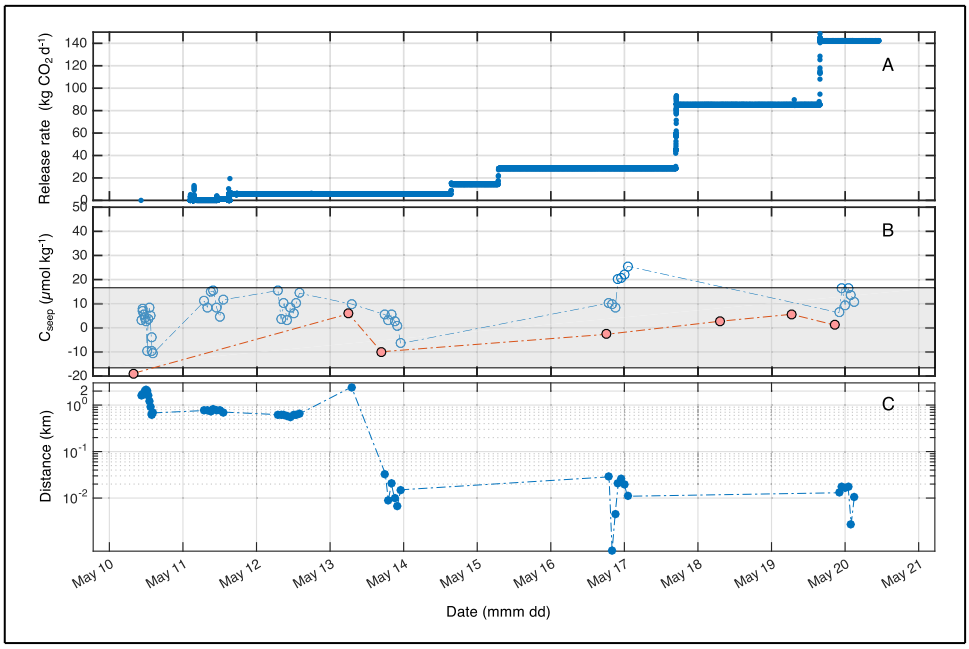

Fig. 9. Temporal development of: (A) mass flow rate of the CO_2 release, and (B) C_{seep}, i.e. the excess C resulting from released−CO_2 dissolved in the sampled seawater. Data sampled by the pumping technique (section 2) are shown in blue, those sampled above the seafloor with Niskin bottles are shown in filled circles. (C) Lateral distance (accuracy ±2.6 m) between the sampling point and location of the initial CO_2 bubble stream at the seafloor.

unequivocally detects the released−CO_2 for moderate-to-high CO_2 release rates > 15 kg d^{-1}. For low CO_2 release rate ≤ 5 kg d^{-1}, C_{seep} values were essentially indistinguishable from zero. The detection of the released−CO_2 signals is based on the DT_{sensor} criterion. However, the fact that the identified signals are in line with other parameters such as the onset of the CO_2 release, current direction, and the strength of the CO_2 release rate lends confidence to the detected signals.

4.3. C_{seep} computed from the cruise data

To evaluate Eq. 9 for the cruise observations, we used the mean C_b value obtained for the POS527 data (2157 µmol kg^{-1}), while ΔC^M_{nat} values were computed from the monitoring datasets POS534P and POS534B. The baseline and monitoring datasets were acquired on different cruises (Tables 1 and 3), but we assumed no systematic errors in the measurements and applied a DT_{cruise} = 16.6 µmol kg^{-1} (section 3.3). The temporal development of the resulting C_{seep} values together with those of the CO_2 release rate and the distance between the sampling point and the CO_2 bubble stream at the seafloor are shown in Fig. 9.

For the POS534B data (sampled through Niskin bottles), no distinct C_{seep} maxima were observed and all values were within the DT_{cruise}. For POS534P (sampled through pumping), on the other hand, C_{seep} values above the threshold were observed on the night shift of May 16–17 (Fig. 9B). There was also a distinct local maximum of C_{seep} on the night shift of May 19–20, but this did not rise over the threshold. Based on the DT_{cruise} criterion, the application of the C_{seep} method on this dataset identified a CO_2 release signal only on May 16–17. However, *RV Poseidon* was investigating the released−CO_2 plume from late May 13 (Fig. 9C), and the local C_{seep} maximum on May 19–20 was probably due to released−CO_2. In any case, it is interesting to note that this local maximum occurred when the CO_2 release rate was three times higher than May 17. It seems, therefore, that the cruise data did not capture the CO_2 release signal as good as the sensor data (Fig. 8) even for high CO_2 release rates. Consequently, false negatives might occur more often for the cruise data. Possible causes for the seemingly lower sensitivity of the cruise data are discussed in section 5.2.

There is also one C_{seep} value (-18.8 µmol kg^{-1}) that exceeds the negative side of DT_{cruise}. This is interpreted as an outlier and indicates that a DT_{cruise} = 19 µmol kg^{-1} is more suitable for this data probably because data acquisition on different cruises introduced additional errors in the model inputs. Note, however, that a higher DT_{cruise} value would increase the risk of false negatives even more.

Finally, the above identification of released−CO_2 signal was based solely on DT_{cruise}, which depends on the remnant variability in C_b. This means that with the availability of a DT value, the application of the C_{seep} method does not require any pre-knowledge of whether there is a seepage occurring nor its eventual whereabouts. However, any additional information available about the seepage situation is very useful to assess the confidence of the results.

5. Discussion

5.1. Implementation flexibility

The modular nature of the C_{seep} method gives the possibility of implementing it at different complexities depending on the purpose of the computations. Some examples of this are provided below.

In this work, the aim was to detect CO_2 seepage signal in addition to quantifying the concentration of excess CO_2 dissolved in the sampled seawater. Thus, we implemented the method in its most rigorous form in four modules by (i) setting up a model that includes as many as possible processes known to influence C concentration in the study area (section 2); (ii) establishing a baseline C through minimising the natural variability (section 3.2); (iii) determining a detection threshold (section 3.3); and (iv) quantifying C_{seep} by evaluating Eq. 9 using C_b and ΔC^M_{nat} values computed from baseline and monitoring data, respectively (section 4). This implementation can be most relevant during the monitoring phase of CCS projects when both identification of anomalous concentration and quantification of the dissolved CO_2 are necessary.

If only determination of C_b is needed, for instance, during site characterisation phase of CCS projects when baseline gathering and understanding/identification of governing processes are the focus, then only the first and second modules of the method need to be implemented. In other cases, the determination of the detection threshold in addition to C_b might be necessary. This can be important for modelling purposes for example. In fact, the recent works of Hvidevold et al. (2015,

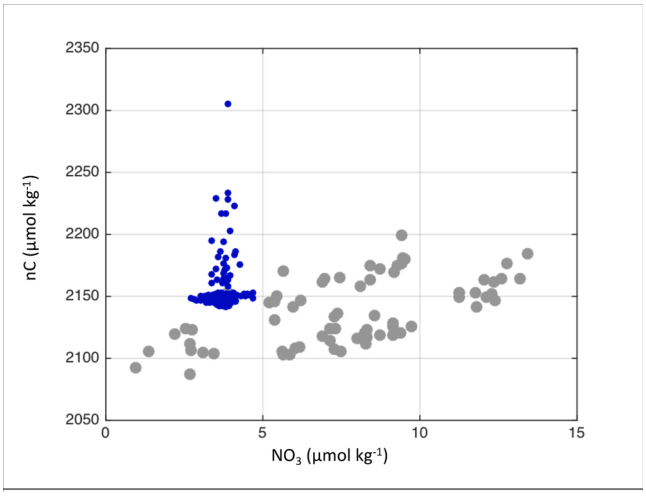

Fig. 10. Concentration of salinity normalized C (nC) plotted against that of nitrate (NO_3) using data from baseline cruises (POS518, POS527, and historical cruises; grey) and the CO_2 release sensor data JC180BBL (blue). Samples contaminated by the released−CO_2 in the JC180BBL data clearly deviate from the slope of the C:N stoichiometry of the data from the baseline cruises.

2016), Alendal (2017) and Oleynik et al. (2020), which investigated optimal sensor placement during seepage CO_2 detection, used the C_{seep} method to define a DT. In such cases, the first three modules should be implemented with DT determined by considering the total error E_{Cseep}. Furthermore, as an additional flexibility, the threshold can be chosen by the user as $\mu_{\_ECseep}+k\sigma_{\_ECseep}$, k = 1, 2 or 3 depending on how important it is to avoid false positives and false negatives. In this work, the threshold was set using k = 2 (section 3.3), increasing k to 3 would increase the occurrence of false negatives, whereas using k = 1 would increase false positives. Apart from determining DT, executing the first three modules determines the level of remnant variability in C_b, analyses its sources, and quantifies its contribution to DT through $\sigma_{\_ECseep}$. In this way, the user is informed about changes in C_b not explained by the underlaying model and their effect on DT.

In situations where the purpose is to quickly check for 'unusual' CO_2 concentrations, the C_{seep} method can be implemented as property-property plots of parameters that are indicative of the main processes of interest. For instance, if the main processes governing C variability at the site are organic matter cycling and CO_2 seepage, then a plot of salinity normalized C (nC) versus nutrients may be used as a seepage CO_2 check. Organic matter cycling produces covariation between nC and nutrients with fairly well constrained slopes, whereas CO_2 seepage increases C without impacting nutrients. Thus, samples contaminated with significant seepage CO_2 will clearly deviate from the slope defined by the nC-nutrient stoichiometry as illustrated in Fig. 10. Other equivalent plots can also be used, such as nC versus apparent oxygen utilization (AOU). In this regard, Uchimoto et al. (2017; 2018) proposed a seepage CO_2 detection method based on purely statistical covariance between seawater pCO_2 and DO. The existence of such covariance, however, most probably stems from the stoichiometric relationship between C and AOU, although not explored in Uchimoto et al. (2017; 2018). It is important to understand that the above mentioned implementation only offers a way to check for anomalous C concentration that do not stem from salinity changes (i.e., mixing/circulation) and/or organic matter cycling. It does not offer any further check of whether the anomalies occur (solely or partly) due to other natural processes, e.g., in-situ dissolution of $CaCO_3$ and/or air-sea gas exchange. Therefore a comprehensive modelling of all the important natural mechanisms influencing C, such as in the full implementation of the C_{seep} method, is necessary.

It is also important to point out that the C_{seep} method is designed for real marine monitoring situations, which can be more complicated and challenging than the current release experiment. During monitoring of CCS sites one might not know if seepage is occurring or not, whereas during the experiment we knew where and when to look for a seepage signal. Furthermore, during the experiment, the baseline and monitoring data were acquired simultaneously and at different (but close) locations. Therefore, the difference between the baseline and monitoring C data resulting from natural variability, i.e., ΔC_{nat}, was small and mostly contributed to by ΔC_{omc}. Consequently, as soon as a signal of high C concentration was observed one could intuitively assume (with some confidence) it stems from the CO_2 release. In real monitoring situations, however, spatial and temporal difference between the baseline and monitoring data can be much larger. This, in turn, will produce larger ΔC_{nat}, which might be contributed to by several processes and even conceal the seepage CO_2 signal. Therefore, in real marine monitoring situations, it is essential to model all of the significant natural processes that influence C, such as in the complete implementation of the C_{seep} method.

Finally, we note the trade-off involving in the above-implied flexibility regarding the timing of baseline data collection relative to the monitoring data. In section 4, we suggested DT_{cruise} larger than DT_{sensor} was more suitable because baseline and monitoring were collected nearly simultaneously for the sensor data, while for the cruises data collection took place in different years. Furthermore, sensitivity calculations showed that if we were to calculate C_{seep} from JC180BBL using the average C_b value obtained from the historical cruise data collected in May 2002 then a $DT_{sensor} \approx 30$ µmol kg^{-1} would be required. This indicates some of the long-term natural C changes were not captured by the current underlying model, and with such elevated DT value the released−CO_2 signal would be captured only during the periods with higher CO_2 release rate (> 80 kgC d^{-1}, Fig. 8). This calls for improved estimate of the long-term C trend in order to assure reliable detection of signals from lower seepage rates as well. To minimise potential error in the long-term trend, baseline data should be up-to-date. This is not necessarily a cumbersome task since any monitoring data that do not reveal CO_2 seepage can be used to update the baseline.

5.2. *Importance of distance to the seepage source, sampling frequency, and measurement accuracy*

An interesting finding from the results presented in section 4 is that although the experimental cruise data measured with benchtop instrumentation (POS534) is more accurate than the in situ sensor data (JC180BBL) (Tables 1 and 3), the latter captured the CO_2 release signal more clearly. For instance, the C_{seep} peak values from JC180BBL were more regular, in phase with the current velocity, and scaled with the CO_2 release rate. A comprehensive analysis of this issue is beyond the scope of this work, but we note two factors that seem to be important. The first is the relative locations of the seepage source and the sensor, with respect to the currents, which is a key factor to take into account. In particular, the sensor data showed a strong vertical gradient. The C_{seep} values were based on samples taken through two inlets: at 17 cm and 87 cm above the seafloor (section 4.1) with an average depth of 119.5 m. At the lower inlet C_{seep} values above DT_{sensor} were between 18 and 170 µmol kg^{-1} whereas for the upper inlet the corresponding C_{seep} values were much lower, 17–74 µmol kg^{-1} (Fig. 8B) This indicates that released−CO_2 signal was nearly double at the lower inlet compared to 70 cm higher. The average sampling depth of POS534P data that were acquired at the experimental site was 116.4 m (114.3–117.4 m) and, thus, around 3 m shallower than the JC180BBL data. This is probably the main reason for the lower C_{seep} values computed for the former dataset (Fig. 9B versus Fig. 8B). Nevertheless, it is worth mentioning that C_{seep} values for the POS534P data on 19–20 May were lower than those on 16–17 May (Fig. 9B). This is despite the facts that on the 19th–20th the CO_2 release rate was higher and the average sampling depth was a metre lower. On both days the hydrodynamic conditions and ship position were very

similar. This suggests, at least for the cruise data, distance to the source alone does not explain the strength of the signal.

The other important factor is the sampling frequency and its effect can be appreciated from the observation that we could not identify any release CO_2 signal in the Niskin bottle data (POS534B) although its analytical method had the best resolution of all the datasets. Therefore, given similar hydrographic settings and distance to the CO_2 seepage source, high-frequency data suits better for capturing the quickly changing seepage signal.

Measurement precision and accuracy are also prerequisites for accurate C_{seep} values as illustrated by the following final example. The contribution of $CaCO_3$ precipitation/dissolution to the natural C variations around the Goldeneye site is generally small (Table 2 and Fig. A1C). However, we cannot rule out the possibility that its importance became significant during the CO_2 release experiment due to potential $CaCO_3$ dissolution in the sediment. If such a dissolution took place and if reaction products entered into the water column in significant amounts, then TA would increase in the water column. This would, in turn, increase ΔC_{CaCO3} values in the monitoring data, which would make a positive contribution to C_{seep}. The experimental TA data from the water column (POS534, JC180BBL) did not show any systematic TA increase in connection with the CO_2 release. However, the effect of $CaCO_3$ dissolution on TA might have not been captured due to noise in the sensor TA data (Appendix B, and Fig. B1B) and low resolution of the cruise data. Thus, TA sensor data with high precision/accuracy is needed to confidently monitor the importance of ΔC_{CaCO3}.

For up-to-date information on commercially available sensors that can deliver the data necessary for C_{seep} computation, we refer the reader to the International Carbon Coordination Project (IOCCP) which promotes, among others, the development of measurement technology for marine biogeochemistry. On the IOCCP website (http://www.ioccp.org) there is a directory of commercially available hardware (sensors and instruments), references listing documents on standards, best practices and user guides, etc.

5.3. Future outlooks for reducing the C_b variability

Several ways to improve modelling ΔC_{nat} need to be tested in the future to reduce the remnant variability in C_b and keep DT as low as possible. For instance, improvement of the uncertainties in dPA/dS and PA_0 maybe be sought by assuming several water mass end-members instead of the two used in the current analysis (section A.3). Also, using equilibrium C value computed from parameters not impacted by CO_2 seepage such as S, TA (obtained from S, as in Eq. A5), T, and atmospheric pCO_2 using the CO2SYS package (van Heuven et al., 2011) has the potential to improve the long-term trend. This also minimises the concern of potential contamination in C_b by seepage CO_2. Lastly, site-specific C_b value may be taken from outputs of well-calibrated regional biogeochemical models. This is specially desirable in situations when it is difficult to acquire new CO_2 seepage-free baseline data. Observational data from open databases, such as GLODAP v2 (Olsen et al., 2016) and SOCAT (https://www.socat.info), will be an asset to calibrate the models.

6. Summary and concluding remarks

In this work we analysed baseline data from historical and recent cruises as well as monitoring data from the first-ever CO_2 release experiment in the north-western North Sea, carried out as part of the EU project STEMM−CCS. We successfully demonstrated the ability of the C_{seep} method to (i) adequately predict natural C variations around the Goldeneye site, over seasonal to interannual time scales; (ii) establish a process-based baseline concentration (C_b) with minimal variability; (iii) determine CO_2 seepage detection threshold and reliably differentiate released−CO_2 from natural variability; and (iv) quantify released−CO_2 dissolved in the sampled seawater (C_{seep}) with concentrations above a pre-defined threshold.

In addition to the above mentioned utilities, we also showed that the C_{seep} method can be implemented in modules depending on the purpose, and with the availability of detection threshold it does not require prior knowledge of CO_2 seepage. Furthermore, the detection threshold used in this study ranged 16.6–19.0 μmol kg^{-1}, which was 18–20 % of the observed natural variability in the study area (Fig. 5), illustrating the high sensitivity of the method. Therefore, the C_{seep} method can be used to monitor large areas by employing pre-defined detection thresholds, C_b value(s), and mobile platforms, e.g., autonomous underwater vehicles equipped with fast-response sensors.

Based on the above results, we conclude that the C_{seep} method features high sensitivity, automation suitability, and with a pre-defined detection threshold, it requires no pre-knowledge of seepage occurrence. Thus, it represents a powerful future monitoring tool both for large and confined marine areas.

Current CCS monitoring requirements comprise of five steps (Dixon and Romanak, 2015): background (baseline) measurements, assessment of CO_2 storage performance in the reservoir, detection of leakage, and (if leakage is detected, suspected or alleged) quantification of leakage and impact assessment. A particular strength of the C_{seep} method is that, if used as a water column monitoring tool, it can address several of the above requirements. Other methods were also tested during the STEMM−CCS project to detect, attribute, and quantify the CO_2 release. For instance, natural tracers that are inherent to the injected CO_2 ($\delta^{13}C_{CO2}$, $\delta^{18}O_{CO2}$) and artificial tracers added to it (Kr, SF_6, C_3F_8) were tested to identify anomalies originating from the released-CO_2 rather than natural sources (Flohr et al., 2021). Studies on the presentations and comparisons of the performance of the different methods are underway and expected to enter the scientific literature soon.

Authors' contribution

Abdirahman M. Omar: conceptualization, methodology, data curation, coding, formal analysis, writing – original draft including visualization.

Maribel I. García-Ibáñez: methodology, coding, writing – reviewing and editing.

Allison Schaap: sensor data curation, writing – reviewing, editing and language.

Anna Oleynik: methodology, coding, writing – reviewing and editing.

Mario Esposito: cruise data curation, writing – reviewing and editing.

Emil Jeansson: data analyses, writing – reviewing and editing.

Socratis Loucaides: sensor data curation, writing – reviewing and editing.

Helmuth Thomas: historical data curation, writing – reviewing and editing.

Guttorm Alendal: writing – contextualization, reviewing, and editing.

Declaration of Competing Interest

None.

Acknowledgement

This work has received funding from the European Union's Horizon 2020 research and innovation programme (contract No. 654462, STEMM-CCS), the ACT programme (Accelerating CCS Technologies, Horizon2020 project No 294766, the ACTOM project), and the Research Council of Norway (Project No. 254711, BayMoDe). H. Thomas acknowledges support by the German Academic Exchange Service (DAAD, #57429828) from funds of the German Federal Ministry of Education and Research (BMBF).We acknowledge Martin Arundell, Stathys Papadimitriou, Matthew Mowlem, John Walk, and Chris Cardwell at the

National Oceanography Centre for the development of the in-situ pH sensors used during the release experiment. We would like to thank the Captains and the crew on *RV Poseidon* for their excellent support during the three expeditions. Thanks also to André Mutzberg, Dominik Jasinski and Maria Martinez-Cabanas at GEOMAR for their help with sampling and measuring nutrients and carbonate parameters. We are also grateful for two anonymous referees who's comments and suggestions improved the manuscript.

Appendix A. Contributions of natural C variability (ΔC_{nat})

In the following subsections, we describe the details on how the components of ΔC_{nat} (ΔC_{omc}, ΔC_{CaCO3}, ΔC_{mix}, and ΔC_{ase}) are computed (Fig. 4). It must be noted that here we are not interested in quantifying ΔC_{nat} integrated over a given period (e.g., one year). Rather, we are interested in quantifying how much (the contribution) each component of ΔC_{nat} caused the measured C concentration to deviate from the theoretical, nominally constant value of C_b that should exist for a given reference value of S, phosphate (PO_4), PA and ΔC_{ase} (Table 2).

A.1 Biology-driven variability

A.1.1 Contribution of organic matter cycling

The formation of organic matter through photosynthesis takes up C and nutrients from seawater, whereas the decay of organic matter through respiration releases C and nutrients back to seawater. Moreover, changes in C and nutrients during photosynthesis and respiration take place in stoichiometric ratios (e.g., Anderson and Sarmiento, 1994; Redfield, 1934; Redfield et al., 1963). Therefore, we quantified the change in C related to photosynthesis and respiration (ΔC_{omc}) using observed changes in phosphate (PO_4) relative to the reference value PO_4^{ref} (Table 2) and the stoichiometric ratio between C and PO_4 (R_{CP}) according to:

$$\Delta C_{omc} = R_{CP}\left(PO_4 - PO_4^{ref}\right) \quad \text{(A1)}$$

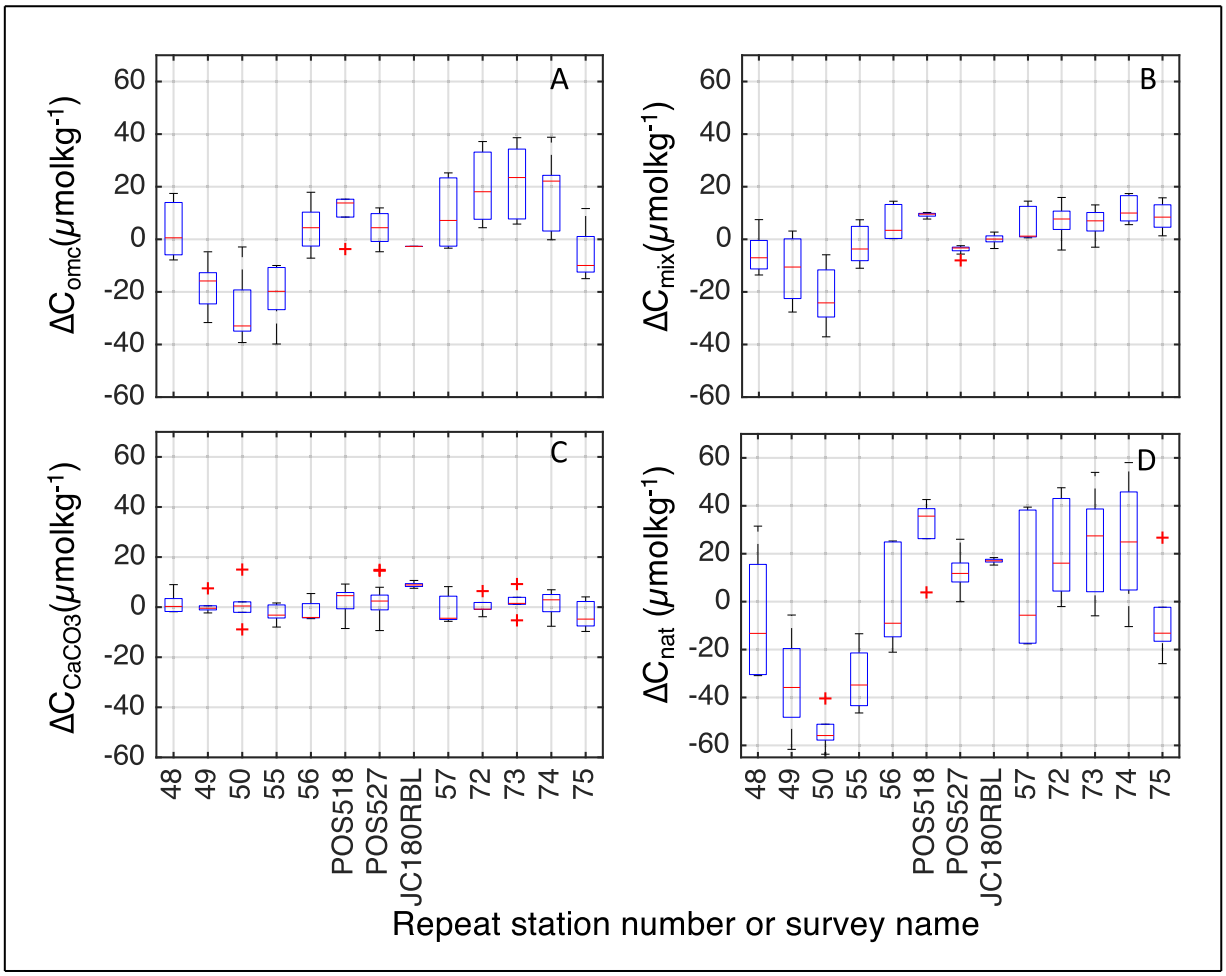

Fig. A1. Modelled contributions of the natural C changes (ΔC_{nat}) arising from the following individual processes: (A) organic matter cycling ($\Delta C_{omc} < 0$: production, $\Delta C_{omc} > 0$: respiration relative to the reference PO_4 in Table 2); (B) salinity changes, i.e. mixing between water masses (ΔC_{mix}); (C) calcium carbonate cycling ($\Delta C_{CaCO3} < 0$: formation, $\Delta C_{CaCO3} > 0$: dissolution relative to the reference PA in Table 2); and (D) ΔC_{nat}, i.e., the sum of the above contributions plus ΔC_{ase}. For each box, the central mark is the median, the edges of the box are the 25th and 75th percentiles, the whiskers extend to the most extreme data points not considered outliers, and outliers are crosses.

We used R_{CP} value of 117 ± 16, which brackets the different values reported in the literature (Redfield, 1934; Anderson and Sarmiento, 1994; Körtzinger et al., 2001).

The resulting values for ΔC_{omc} are shown in Fig. A1 A and these range from -40 to +40 μmol kg^{-1}. Generally, the shallow near-coast stations (49, 50, and 55; Fig. 3) show net organic matter production relative to the reference state (Table 2), while the rest of the stations show either net respiration or a balance between respiration and photosynthesis.

A.1.2 Contribution of calcium carbonate ($CaCO_3$) cycling

In situ formation (dissolution) of $CaCO_3$ structures remove (release) CO_3^{2-} from (to) seawater and therefore decrease (increase) TA and C according to Eqs. 1 and 2. The resulting TA and C changes occur in a stoichiometric ratio of 2:1 (Zeebe and Wolf-Gladrow, 2001). Consequently, TA data can be used to (i) monitor the in situ $CaCO_3$ changes, and (ii) quantify the resulting C change (ΔC_{CaCO3}) using (e.g., Brewer, 1978):

$$\Delta C_{CaCO_3} = 0.5 * \left(\mathrm{nPA} - \mathrm{PA}^{S^{ref}}\right) \tag{A2}$$

where PA is the potential TA computed from the measured TA and nitrate (NO_3) following Kanamori and Ikegami (1982) and Wolf-Gladrow et al. (2007):

$$\mathrm{PA} = \mathrm{TA} + 1.36{*}\mathrm{NO_3} \tag{A3}$$

In Eq. A2, nPA is salinity normalized PA (Friis et al., 2003):

$$\mathrm{nPA} = \frac{(\mathrm{PA} - \mathrm{PA_0}){*}\mathrm{S}^{ref}}{\mathrm{S}} + \mathrm{PA_0} \tag{A4}$$

$PA^{S^{ref}}$ is the theoretical PA predicted for the reference salinity (S^{ref}) (Table 2). To determine $PA^{S^{ref}}$ we regressed computed PA with salinity and the best fit equation was:

$$\mathrm{PA} = \frac{d\mathrm{PA}}{d\mathrm{S}}\mathrm{S} + \mathrm{PA_0} \tag{A5}$$

where the slope dPA/dS = 67.5 ± 7.4 μmol kg^{-1} and the intercept PA_0 =-46 ± 261 μmol kg^{-1}. Note, the fact that our observational data do not include TA values for freshwater and/or brackish water results in the high uncertainty of the intercept.

Eq. A5 and S^{ref} = 35.1 were used to compute $PA^{S^{ref}}$ (Table 2). Moreover, the predicted PA value at zero salinity (PA_0) was determined from the intercept of Eq. A5.

The resulting values for ΔC_{CaCO3} were generally less than ±10 μmol kg^{-1} (Fig. A1C) and were insignificant compared ΔC_{omc} (Fig. A1A).

A.2 Air-sea gas exchange-driven variability

At the air-sea interface, CO_2 is exchanged between atmosphere and ocean. The direction of the flux is dictated by the CO_2 partial pressure difference between surface seawater and the overlaying air ($\Delta pCO_2 = pCO_{2air} - pCO_{2sea}$). The CO_2 flux is from (to) the atmosphere towards (from) the ocean if $\Delta pCO_2 > 0$ ($\Delta pCO_2 < 0$). Furthermore, the strength of the flux scales with wind speed (e.g., Sweeney et al., 2007). This process influences C in two ways. First, fluctuations in ΔpCO_2 and/or in wind speed cause fluctuations in C in the surface water and some of this signal could be transported to the deeper waters. However, given that the northern North Sea is seasonally stratified, this fluctuation has only a strong impact on the surface water and we thus neglect its effect in this work. Second, since we are using data covering a long period (18 years), accumulation of anthropogenic CO_2 (C_{ant}) is expected to steadily increase C over time. The rate of this increase could not be discerned from the low-resolution data we used here. However, Omar et al. (2019) analysed a decade of underway surface data in the northern North Sea and reported an annual C increase of 1.2 ± 0.3 μmol kg^{-1} yr^{-1}. The addition of C_{ant} does not necessarily take place locally in the North Sea, but can be carried by advection of water masses into the region, e.g., with the inflow of North Atlantic Water and, therefore, should be expected to impact also the deep waters. Thus, we used the estimate of Omar et al. (2019) to adjust all C data to the year 2010 according to:

$$\Delta C_{ase} = C_{ant} = 1.2{*}(\mathrm{yr} - 2010) \tag{A6}$$

where yr is the year of observation.

For the historical C values, ΔC_{ase} values ranged between -10.8 and 1.2 μmol kg^{-1}. For the C data acquired in 2017, 2018, and 2019 ΔC_{ase} values were 8.4, 9.6, and 10.8 μmol kg^{-1}, respectively.

A.3 Mixing-driven variability

Mixing of water masses changes the distribution of C and TA in the water column. Here, we consider the PA–S linear relationship in Eq. A5 to be the result of mixing between low-salinity Coastal Water and high-salinity North Atlantic Water. Other water mass end-members maybe contributing to the observed S relationship, but the effect of this is accounted for through the substantial uncertainties in the regression coefficients of Eq. A5.

Measured C is not a conservative parameter because of the sinks/sources driven by ΔC_{bio} and ΔC_{ase}. However, once the fluctuations arising from ΔC_{bio} and ΔC_{ase} are accounted for we assume that the resulting modified C mix conservatively just like PA (above). Therefore, we computed the contribution of salinity changes (ΔC_{mix}) using the difference between measured and reference salinity and the slope of Eq. A5:

$$\Delta C_{mix} = \mathrm{dPA/dS}\ (\mathrm{S} - \mathrm{S}^{ref}) \tag{A7}$$

Finally, C_b was calculated as

$$C_b = C - (\Delta C_{bio} + \Delta C_{ase} + \Delta C_{mix}) = C - \Delta C_{nat} \quad (A8)$$

where the terms in parenthesis are by definition ΔC_{nat}. As can be seen from Fig. A1B, values of ΔC_{mix} range between –40 and 20 μmol kg^{-1} and are lower for the coastal water stations. This means that higher C adjustments were necessary for the low-salinity coastal water to be brought to C levels corresponding to reference samples with S = 35.1.

Appendix B. Circumvention of data coverage and quality limitations

The monitoring and baseline datasets JC180BBL and JC180BL, respectively, included some differences in temporal coverage and data quality as depicted in Fig. B1. The following limitations are notable from the graphs:

First, salinity was measured only at the JC180BL lander (Fig. B1A). We circumvented this limitation by using the same salinity values for both sites, i.e. we implicitly assumed that there was no significant systematic salinity difference between the two sites, which are < 0.5 km apart (Fig. 3). A comparison between the salinity of the deepest samples in the POS534P dataset (Fig. B1A, black dots) and those measured at the JC180BBL lander (Fig. B1A, navy dots), when *RV Poseidon* was up to 1 km away from the lander, showed practically indistinct salinity values supporting the above assumption. For example, the largest observed deviation of 0.05 would produce a 3.4 μmol kg^{-1} difference in PA (according to Eq. A5) and 1.7 μmol kg^{-1} difference in C_b (according to Eq. A7). Both these changes are way lower than other uncertainties involved in the determination of the C_{seep} (section 3.3).

Second, TA values from the JC180BBL dataset were highly noisy (Fig. B1B, navy dots). This could partly result from regular disturbance of sediment sampling activity conducted with a ROV moving around and inserting/removing sediment-based instruments quite close to the sensors for TA and PO4 (below). This could have caused pore waters with higher TA and PO4 to mix into the water column occasionally. In any case, we dealt with the noise by using the average value of TA (2333 μmol kg^{-1}) measured at JC180BL. This is a reasonable approximation given that (i) mean values of the TA values from the two landers are essentially indistinguishable (2309 ± 56 μmol kg^{-1} vs. 2333 ± 5 μmol kg^{-1}), and (ii) TA is mainly a function of S and we used the same S values for both sites (above).

Third, PO_4 values from the JC180BBL dataset are noisier than their JC180BL counterparts (Fig. B1D) probably due to the same reasons as in the TA data (above). Furthermore, from Fig. B2 we noticed that while all cruise data falls around a line defining the stoichiometric relationship known to exist between PO_4 and NO_3 (e.g., Redfield, 1934; Redfield et al., 1963; Anderson and Sarmiento, 1994), the sensor data deviates from this relationship, especially for high PO_4 values. We also noticed that, according to the cruise data, PO_4 values higher than 1 μmol kg^{-1} are not typical for the study area. Thus, we considered any sensor PO_4 values higher than 0.8 μmol kg^{-1} as suspicious. This also implies that some of PO_4 variability of the sensor data is noise. Thus, for the computation of C_b (section 3.2) in the JC180BL data we used the average PO_4 (0.6 μmol kg^{-1}) based on values ≤0.8 μmol kg^{-1}.

Fourth, we also noted that NO_3 values from the JC180BBL dataset are systematically lower than those from the JC180BL by around 1 μmol kg^{-1} (Fig. B1C). On the other hand, PO_4 values from the JC180BBL are higher than those from JC180BL. We considered the the less noisy JC180BBL NO_3 measurements to be more trustworthy. Therefore, for the computation of ΔC^{M}_{nat} from JC180BBL data (section 4.2) we used a PO_4 value of 0.41 μmol kg^{-1} calculated from the average NO_3 concentration (3.74 μmol kg^{-1}) using the relationship defined by the cruise data (Fig. B2).

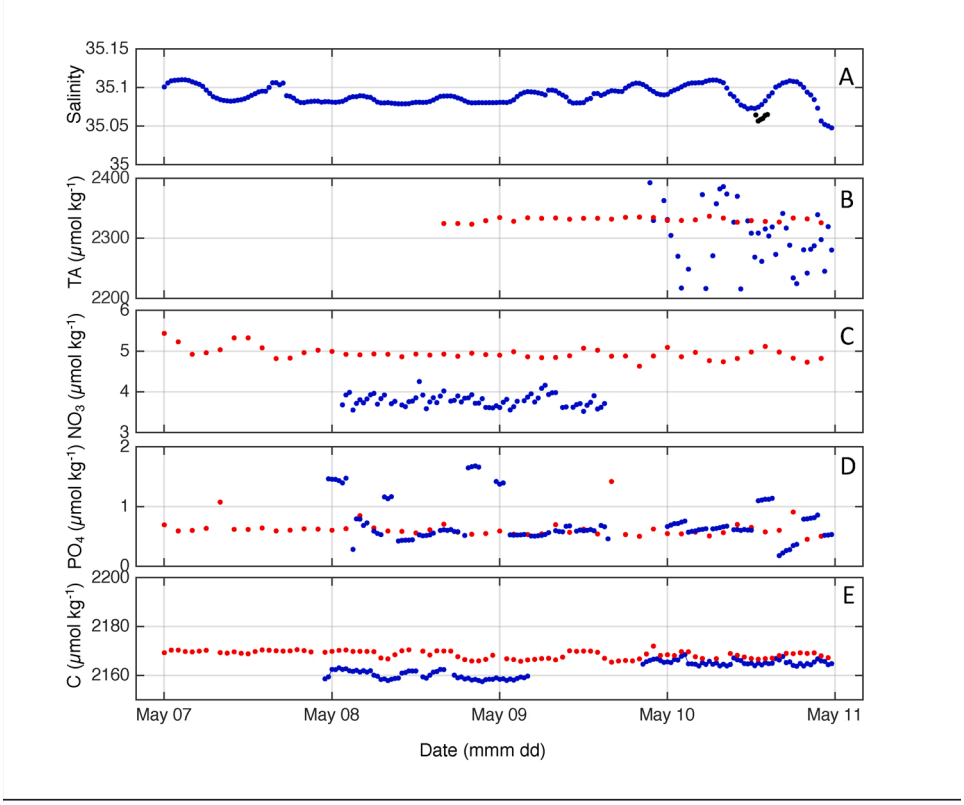

Fig. B1. Four days long example of: measured (A) S, (B) TA, (C) NO_3, (D) PO_4, and (E) computed C. JC180BL data points are shown in red, JC180BBL in navy blue. Also shown are measured deep water S for POS534P (A, black) when *RV Poseidon* was 0.6 to 1.6 km away from the JC180BBL lander.

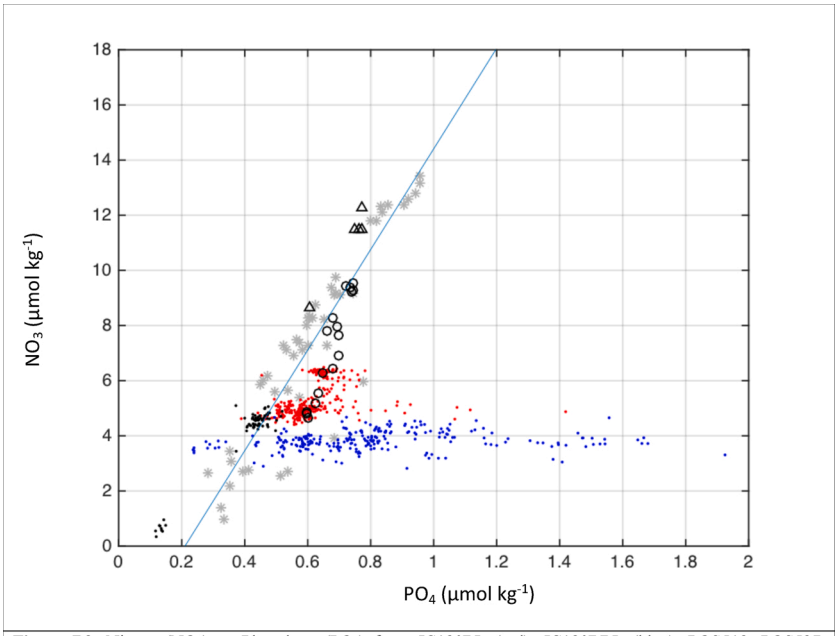

Fig. B2. Nitrate (NO_3) vs Phosphate (PO_4) from JC180BL (red), JC180BBL (blue), POS518, POS527, POS534 (black), and historical cruises (grey). Blue dots demonstrate that NO_3 and PO_4 are decoupled for the sensor data. The solid line indicates the best fit for all cruise data, $NO_3 = 18.3(\pm 1)*PO_4 - 3.84(\pm 0.7)$.

References

Alendal, G., 2017. Cost efficient environmental survey paths for detecting continuous tracer discharges. J. Geophys. Res. Oceans 122 (7), 5458–5467. https://doi.org/10.1002/2016JC012655.

Anderson, G.M., 1976. Error propagation by the Monte Carlo method in geochemical calculations. Geochim. Cosmochim. Acta 40, 1533–1538.

Anderson, L.A., Sarmiento, J.L., 1994. Redfield ratios of remineralization determined by nutrient data analysis. Global Biogeochem. Cycles 8, 65–80. https://doi.org/10.1029/93GB03318.

Beaton, A.D., et al., 2012. Lab-on-Chip measurement of nitrate and nitrite for in situ analysis of natural waters environ. Sci. Technol. 46, 9548–9556. https://doi.org/10.1021/es300419u.

Blackford, J.C., Artioli, Y., Clark, J., de Mora, L., 2017. Monitoring of offshore geological carbon storage integrity: implications of natural variability in the marine system and the assessment of anomaly detection criteria. Int. J. Greenh. Gas Control. 64, 99–112. https://doi.org/10.1016/j.ijggc.2017.06.020.

Blackford, J., Alendal, G., Avlesen, H., Brereton, A., Cazenave, P.W., Chen, B., et al., 2020. Impact and detectability of hypothetical CCS offshore seep scenarios as an aid to storage assurance and risk assessment. Int. J. Greenh. Gas Control. 95, 102949 https://doi.org/10.1016/j.ijggc.2019.102949.

Bockmon, E.E., Dickson, A.G., 2015. An inter-laboratory comparison assessing the quality of seawater carbon dioxide measurements. Mar. Chem. 171, 36–43. https://doi.org/10.1016/j.marchem.2015.02.002.

Botnen, H.A., Omar, A.M., Thorseth, I., Johannessen, T., Alendal, G., 2015. The effect of submarine CO_2 vents on seawater: implications for detection of subsea carbon sequestration leakage. Limnol. Oceanogr. 60, 402–410. https://doi.org/10.1002/lno.10037.

Brewer, P.G., 1978. Direct observation of the oceanic CO_2 increase. Geophys. Res. Lett. 5, 997–1000.

Bushinsky, S.M., Takeshita, Y., Williams, N.L., Observing Changes in Ocean Carbonate Chemistry, 2019. Our autonomous future. Curr. Clim. Change Rep. 5, 207–220. https://doi.org/10.1007/s40641-019-00129-8.

Clargo, N.M., Salt, L.A., Thomas, H., de Baar, H.J.W., 2015. Rapid increase of observed DIC and pCO2 in the surface waters of the North Sea in the 2001-2011 decade ascribed to climate change superimposed by biological processes. Mar. Chem. 177, 566–581.

Clinton-Bailey, G.S., et al., 2017. A lab-on-Chip analyzer for in situ measurement of soluble reactive phosphate improved phosphate blue assay and application to fluvial monitoring. Environ. Sci. Technol. 51, 9989–9995. https://doi.org/10.1021/acs.est.7b01581.

Connelly, D., et al., 2019. RRS James Cook Cruise JC180 25 April - 30 May 2019. Strategies for the Environmental Monitoring of Marine Carbon Capture and Storage, STEMM-CCS. Southampton, National Oceanography Centre, 63. National Oceanography Centre Cruise Report, p. 193 pp. http://nora.nerc.ac.uk/id/eprint/525651.

Damen, K., Faaij, A., Turkenburg, W., 2006. Health, safety and environmental risks of underground CO_2 storage – overview of mechanisms and current knowledge. Clim. Change 74, 289–318. https://doi.org/10.1007/s10584-005-0425-9.

Dean, M., Blackford, J., Connelly, D., Hines, R., 2020. Insights and Guidance for Offshore CO2 Storage Monitoring Based on the QICS, ETI MMV, and STEMM-CCS Projects. https://doi.org/10.1016/j.ijggc.2020.103120.

DeGrandpre, M.D., Hammar, T.R., Wallace, D.W.R., Wirick, C.D., 1997. Simultaneous mooring-based measurements of seawater CO_2 and O_2 off Cape Hatteras, North Carolina. Limnol. Oceanogr. 42, 21–28. https://doi.org/10.4319/lo.1997.42.1.0021.

Dickson, A.G., 2010. The carbon dioxide system in seawater: equilibrium chemistry and measurements. In: Riebesell, U., Fabry, V.J., Hansson, L., Gattuso, J.P. (Eds.), Guide to Best Practices for Ocean Acidification Research and Data Report. Publications Office of the European Union, Luxembourg, pp. 17–40.

Dickson, A.G., Rilley, J.P., 1978. The effect of analytical error on the evaluation of the components of the aquatic carbon-dioxide system. Mar. Chem. 6, 77–85. https://doi.org/10.1016/0304-4203(78)90008-7.

Dickson, A.G., Sabine, C.L., Christian, J.R., 2007. Guide to best practices for ocean CO_2 measurements. PICES Special Public. 3, 191.

Dixon, T., Romanak, K.D., 2015. Improving monitoring protocols for CO_2 geological storage with technical advances in CO2 attribution monitoring. Int. J. Greenh. Gas Control. 41, 29–40. https://doi.org/10.1016/j.ijggc.2015.05.029.

Esposito, M., Martínez-Cabanas, M., Connelly, D.P., Jasinski, D., Linke, P., Schmidt, M., Achterberg, E.P., 2021. Water Column Baseline Assessment for Offshore Carbon Dioxide Capture and Storage (CCS) Sites: Analysis of Field Data From the Goldeneye Storage Complex Area. Submitted to the current special issue of IJGGC.

European Commission, 2011. Implementation of Directive 2009/31/EC on the Geological Storage of Carbon Dioxide: Guidance Document 2, Characterisation of the Storage Complex, CO_2 Stream Composition, Monitoring and Corrective Measures, p. 2011.

Flohr, A., Schaap, A., Achterberg, E.P., Alendal, G., Arundell, M., Berndt, C., Blackford, J., Böttner, C., Borisov, S.M., Brown, R., Bull, J.M., Carter, L., Chen, B., Dale, A.W., de Beer, D., Dean, M., Deusner, C., Dewar, M., Durden, J.M., Elsen, S., Esposito, M., Faggetter, M., Fischer, J.P., Gana, A., Gros, J., Haeckel, M., Hanz, R., Holtappels, M., Hosking, B., Huvenne, V.A.I., James, R.H., Koopmans, D., Kossel, E., Leighton, T.G., Li, J., Lichtschlag, A., Linke, P., Loucaides, S., Martínez-Cabanas, M., Matter, J.M., Mesher, T., Monk, S., Mowlem, M., Oleynik, A., Papadimitriou, S., Paxton, D., Pearce, C.R., Peel, K., Roche, B., Ruhl, H.A., Saleem, U., Sands, C., Saw, K., Schmidt, M., Sommer, S., Strong, J.A., Triest, J., Ungerböck, B., Walk, J., Paul, P., Widdicombe, S., Wilson, R.E., Wright, H., Wyatt, J., Connelly, D., 2021. Towards improved monitoring of offshore carbon storage: A real-world field experiment detecting a controlled sub-seafloor CO_2 release. Int. J. Greenhouse Gas Control. https://doi.org/10.1016/j.ijggc.2020.103237.

Friis, K., Kortzinger, A., Wallace, D.W.R., 2003. Salinity normalization of marine inorganic carbon chemistry data. Geophys. Res. Lett. 30, 1085. https://doi.org/10.1029/2002GL015898.

Fuss, S., Canadell, J., Peters, G., Tavoni, M., Andrew, R.M., Ciais, P., Jackson, R.B., Jones, C.D., Kraxner, F., Nakicenovic, N., Le Quéré, C., Raupach, M.R., Sharifi, A., Smith, P., Yamagata, Y., 2014. Betting on negative emissions. Nature Clim Change 4, 850–853. https://doi.org/10.1038/nclimate2392.

Global CCS institute, 2019. Global Status of CCS 2019: Targeting Climate Change. Accessed: https://www.globalccsinstitute.com/resources/global-status-report/.

Gundersen, K., Alendal, G., Oleynik, A., Blaser, N., 2020. Binary time series classification with bayesian convolutional neural networks when monitoring for marine gas discharges. Algorithms 13, 145.

Hammond, G.P., 2018. System characterisation of carbon capture and storage (CCS) systems. In: Clair, G., Patricia, T., Sarah, M., Naomi, V., Temitope, F. (Eds.), Biomass Energy With Carbon Capture and Storage (BECCS). https://doi.org/10.1002/9781119237716.ch7.

Hvidevold, H.K., Alendal, G., Ali, A., Johannessen, T., Mannseth, T., Avlesen, H., 2015. Layout of CCS monitoring infrastructure with highest probability of detecting a footprint of a CO2 leak in a varying marine environment. Int. J. Greenh. Gas Control. 37 (June), 274–279. https://doi.org/10.1016/j.ijggc.2015.03.013, 2015.

Hvidevold, H.K., Alendal, G., Johannessen, T., Ali, A., 2016. Survey strategies to quantify optimize detecting probability of a CO2 seep in a varying marine environment. Environ. Model. Softw. (83), 303–309. https://doi.org/10.1016/j.envsoft.2016.06.006.

IEAGHG, 2008. International Energy Agency Greenhouse Gas Research & Development Programme, "Assessment of Sub Sea Ecosystem Impacts". Report No. 2008/8.

IPCC, 2013. In: Stocker, T.F., Qin, D., Plattner, G.-K., Tignor, M., Allen, S.K., Boschung, J., Nauels, A., Xia, Y., Bex, V., Midgley, P.M. (Eds.), Climate Change 2013: The Physical Science Basis. Contribution of Working Group I to the Fifth Assessment Report of the Intergovernmental Panel on Climate Change. Cambridge University Press, Cambridge, United Kingdom and New York, NY, USA, p. 1535.

IPCC, 2018. In: Masson-Delmotte, V., Zhai, P., Pörtner, H.-O., Roberts, D., Skea, J., Shukla, P.R., Pirani, A., Moufouma-Okia, W., Péan, C., Pidcock, R., Connors, S., Matthews, J.B.R., Chen, Y., Zhou, X., Gomis, M.I., Lonnoy, E., Maycock, T., Tignor, M., Waterfield, T. (Eds.), Global Warming of 1.5°C. An IPCC Special Report on the Impacts of Global Warming of 1.5°C Above pre-Industrial Levels and Related Global Greenhouse Gas Emission Pathways, in the Context of Strengthening the Global Response to the Threat of Climate Change, Sustainable Development, and Efforts to Eradicate Poverty. In Press.

Jenkins, C., 2020. The State of the Art in Monitoring and Verification: an update five years on. Int. J. Greenh. Gas Control 100. https://doi.org/10.1016/j.ijggc.2020.103118.

Kanamori, S., Ikegami, H., 1982. Calcium-alkalinity relationship in the North Pacific. J. Oceanogr. Soc. Jpn. 38, 57–62. https://doi.org/10.1007/BF02110291.

Körtzinger, A., Koeve, W., Kähler, P., Mintrop, L., 2001. C:N ratios in the mixed layer during the productive season in the northeast Atlantic Ocean. Deep. Sea Res. Part I Oceanogr. Res. Pap. 48, 661–688. https://doi.org/10.1016/S0967-0637(00)00051-0.

Lawrence, M.G., Schäfer, S., Muri, H., Scott, V., Oschlies, A., Vaughan, N.E., Boucher, O., Schmidt, H., Haywood, J., Scheffran, J., 2018. Evaluating climate geoengineering proposals in the context of the Paris Agreement temperature goals. Nat. Commun. 9, 3734. https://doi.org/10.1038/s41467-018-05938-3.

Linke, Peter, Schmidt, Mark, Rohleder, Marco, Al-Barakati, Alaa, Al-Farawati, Radwan, 2015. Novel online digital video and high-speed data broadcasting via standard coaxial cable onboard marine operating vessels. Mar. Technol. Soc. J. 49 (1), 7–18. https://doi.org/10.4031/MTSJ.49.1.2, 785.

Millero, F.J., 2007. The marine inorganic carbon cycle. Chem. Rev. 107 (2), 308–341. https://doi.org/10.1021/cr0503557.

Millero, F.J., Graham, T.B., Huang, F., Bustos-Serrano, H., Pierrot, D., 2006. Dissociation constants of carbonic acid in seawater as a function of salinity and temperature. Mar. Chem. 100, 80–94.

Oleynik, A., Alendal, G., Omar, A., Blaser, N., García-Ibáñez, M.I., 2020. Optimal sensors placement for detecting CO_2 discharges from unknown locations on the seafloor. Int. J. Greenh. Gas Control 95, 102951. https://doi.org/10.1016/j.ijggc.2019.102951.

Olsen, A., Key, R.M., van Heuven, S., Lauvset, S.K., Velo, A., Lin, X., Schirnick, C., Kozyr, A., Tanhua, T., Hoppema, M., Jutterström, S., Steinfeldt, R., Jeansson, E., Ishii, M., Pérez, F.F., Suzuki, T., 2016. The Global Ocean Data Analysis Project version 2 (GLODAPv2) – an internally consistent data product for the world ocean. Earth Syst. Sci. Data Discuss. 8, 297–323. https://doi.org/10.5194/essd-8-297-2016.

Omar, A., García-Ibáñez, M., Alendal, G., 2018. The stoichiometric C_{seep} method as a tool to distinguish CO_2 seepage signal from the natural variability. In: Proceedings for GHGT14. Melbourne. October 2018.

Omar, A.M., Thomas, H., Olsen, A., Becker, M., Skjelvan, I., Reverdin, G., 2019. Trends of ocean acidification and pCO_2 in the northern North Sea, 2003-2015. J. Geophys. Res. 124, 3088–3103. https://doi.org/10.1029/2018JG004992.

Redfield, A.C., 1934. On the Proportions of Organic Derivatives in Sea Water and Their Relation to the Composition of Plankton. James Johnstone Memorial Volume. University Press of Liverpool, pp. 176–192.

Redfield, A.C., Ketchum, B.H., Richards, F.A., 1963. The influence of organisms on the composition of sea-water. In: Hill, M.N. (Ed.), The Composition of Seawater: Comparative and Descriptive Oceanography. The Sea: Ideas and Observations on Progress in the Study of the Seas, 2, pp. 26–77.

Rérolle, V.M.C., et al., 2013. Development of a colorimetric microfluidic pH sensor for autonomous seawater measurements. Anal. Chim. Acta 786, 124–131. https://doi.org/10.1016/j.aca.2013.05.008.

Romanak, K.D., Bennett, P.C., Yang, C., Hovorka, S.D., 2012. Process-based approach to CO_2 leakage detection by vadose zone gas monitoring at geologic CO_2 storage sites. Geophys. Res. Lett. 39, L15405 https://doi.org/10.1029/2012GL052426.

Schaaf, A., Bond, C.E., 2019. Quantification of uncertainty in 3-D seismic interpretation: implications for deterministic and stochastic geomodeling and machine learning. Solid Earth 10, 1049–1061. https://doi.org/10.5194/se-10-1049-2019.

Schmidt, M., 2019. RV POSEIDON Fahrtbericht / Cruise Report POS534 STEMM-CCS: Strategies for Environmental Monitoring of Marine Carbon Capture and Storage Leg 1: Kiel (Germany) – Aberdeen (United Kingdom) 01.05. – 22.05.2019 Leg 2: Aberdeen (United Kingdom) – Bremerhaven (Germany) 23.05. – 29.05.2019. Open Access. GEOMAR Report, N. Ser. 052. GEOMAR Helmholtz-Zentrum für Ozeanforschung, Kiel, Germany, p. 51. https://doi.org/10.3289/geomar_rep_ns_52_2019.

Schmidt, Mark, Linke, Peter, Sommer, Stefan, Esser, Daniel, Cherednichenko, Sergiy, 2015. Natural 843 CO_2 seeps offshore panarea: a test site for subsea CO_2 leak detection 844 technology. Mar. Technol. Soc. J. 49 (1), 19–30. https://doi.org/10.4031/MTSJ.49.1.3, 845.

Sweeney, C., Gloor, E., Jacobson, A.R., Key, R.M., McKinley, G., Sarmiento, J.L., Wanninkhof, R., 2007. Constraining global air-sea gas exchange for CO_2 with recent bomb ^{14}C measurements. Global Biogeochem. Cycles 21, GB2015. https://doi.org/10.1029/2006GB002784.

Thomas, H., 2002. Shipboard Report of the RV Pelagia cruises 64PE184, 64PE187, 64PE190 and 64PE195. Netherlands: Royal Netherlands Institute for Sea Research, Texel, NL.

U.S. EPA, 2010. Federal requirements under the underground injection control (UIC) program for carbon dioxide (CO_2) geologic sequestration (GS) wells. Federal Regulation 75 (237), 77230–77303.

Uchimoto, K., Kita, J., Xue, Z., 2017. A novel method to detect CO_2 leak in offshore storage: focusing on relationship between dissolved oxygen and partial pressure of CO_2 in the sea. Energy Proced. 114, 3771–3777. https://doi.org/10.1016/j.egypro.2017.03.1507.

Uchimoto, K., Nishimura, M., Kita, J., Xue, Z., 2018. Detecting CO_2 leakage at offshore storage sites using the covariance between the partial pressure of CO_2 and the saturation of dissolved oxygen in seawater. Int. J. Greenh. Gas Control. 72 (May), 130–137. https://doi.org/10.1016/j.ijggc.2018.03.020.

van Heuven, S., Pierrot, D., Rae, J.W.B., Lewis, E., Wallace, D.W.R., 2011. MATLAB Program Developed for CO_2 System Calculations. ORNL/CDIAC-105b. CDIAC, Oak Ridge National Laboratory, Department of Energy, Oak Ridge, Tennessee, U.S.A. https://doi.org/10.3334/CDIAC/otg.CO2SYS_MATLAB_v1.1.

van Vuuren, D.P., Stehfest, E., den Elzen, M.G.J., Kram, T., van Vliet, J., Deetman, S., Isaac, M., Goldewijk, K.K., Hof, A., Mendoza Beltran, A., Oostenrijk, R., van Ruijven, B., 2011. RCP2.6: exploring the possibility to keep global mean temperature increase below 2°C. Clim. Change 109, 95. https://doi.org/10.1007/s10584-011-0152-3.

Wolf-Gladrow, D.A., Zeebe, R.E., Klaas, C., Körtzinger, A., Dickson, A.G., 2007. Total alkalinity: the explicit conservative expression and its application to biogeochemical processes. Mar. Chem. 106, 287–300. https://doi.org/10.1016/j.marchem.2007.01.006.

Zeebe, R.E., Wolf-Gladrow, D.A., 2001. CO_2 In Seawater: Equilibrium, Kinetics and Isotopes. Elsevier Science, B.V., Amsterdam.